



A multi-decadal dataset of surface damage on Antarctic ice shelves (1999–2024)

Leyue Tang^{1,2}, Jonathan L. Bamber^{2,3}, Tian Li², Gang Qiao¹

¹Center for Spatial Information Science and Sustainable Development Applications, College of Surveying and Geoinformatics, Tongji University, Shanghai 200092, China

²Bristol Glaciology Centre, School of Geographical Sciences, University of Bristol, Bristol, BS8 1SS, UK

³Institute for Advanced Study, Technical University of Munich, Garching, 85748, Germany

Correspondence to: Gang Qiao (qiaogang@tongji.edu.cn)

Abstract. Many Antarctic ice shelves have undergone accelerated thinning and retreat in recent decades, weakening their buttressing effect on grounded ice and increasing the risk of further sea-level rise. Surface damage, including crevasses, rifts and heavily fractured areas, is an important indicator of ice shelf structural integrity, but there is limited understanding of its long-term evolution across Antarctic ice shelves. Here we present a new surface damage dataset for nine representative Antarctic ice shelves, derived from Landsat optical imagery covering the period 1999–2024. These ice shelves include Amery, Brunt, Crosson, Dotson, Holmes, Larsen B, Pine Island, Thwaites and Totten, and encompass a range of change behaviours from relatively stable to rapidly changing systems. A deep-learning image segmentation model was trained on a manually annotated dataset from diverse Antarctic ice shelves to automatically map surface damage. To extend the usable record, Landsat 7 scan-line-corrector-off imagery was restored using a diffusion-model-based framework fine-tuned for Antarctic imagery. The final dataset contains 170 surface damage maps at 30 m resolution, each representing a single ice shelf for a specific year. Temporal coverage varies among ice shelves owing to differences in the availability of usable imagery. The model achieved a mean intersection over union of 0.845 on the test set and 0.822 on an independent validation ice shelf not included in model training. The dataset demonstrates good multi-temporal consistency, supporting its use for time-series analysis. Among the nine ice shelves, Pine Island, Thwaites and Larsen B show the most pronounced surface damage changes during the study period. Compared with existing studies, this dataset provides improved temporal continuity over multi-decadal timescales at substantially finer spatial resolution, offering new insights into the long-term evolution of Antarctic ice shelves and contributing to a better understanding of ice shelf instability. The dataset is publicly available at <https://doi.org/10.5281/zenodo.20425951> (Tang et al., 2026a).

1 Introduction

As the largest reservoir of land ice on Earth, the Antarctic Ice Sheet (AIS) represents the greatest potential contributor to global sea-level rise and the dominant source of uncertainty in future sea-level-rise projections (Fricker et al., 2025). Between 1992 and 2020, the AIS lost $2,671 \pm 530$ Gt of ice mass, contributing 7.4 ± 1.5 mm to global sea-level rise (Otosaka



et al., 2023). The floating ice shelves provide important buttressing to the grounded ice sheet. The thinning and retreat of ice shelves can weaken this buttressing effect, promoting faster inland ice flow and increased ice discharge into the ocean, and thereby increasing the future contribution of the AIS to global sea-level rise (Miles and Bingham, 2024; Bassis et al., 2024). Antarctic ice shelves have undergone substantial changes in recent decades. Between 1997 and 2021, the total area of
35 Antarctic ice shelves decreased by $36,701 \pm 1,465 \text{ km}^2$ (1.9 %), mainly driven by major calving events (Greene et al., 2022). Widespread thinning over the same period has further contributed to Antarctic ice-shelf mass loss (Davison et al., 2023). Continuous monitoring of Antarctic ice shelves is therefore critical for understanding their stability and assessing their future evolution.

Surface damage is an important indicator of ice shelf structural weakening and changes in rheological properties (Colgan et al., 2016). It can weaken ice shelf structural integrity, thereby promoting calving and the associated ice-front retreat (Borstad et al., 2012). Surface damage on ice shelves includes crevasses, rifts and heavily fractured areas, such as intensely fractured zones within shear margins. Damage development is linked to enhanced shear, ice flow acceleration, increased strain rates and ice shelf thinning, with these interactions being climate-sensitive and becoming more pronounced in a warming climate (Izeboud et al., 2025). Studies have shown that damage evolution is closely associated with the disintegration and structural
45 weakening of several major ice shelves, such as Larsen B (Glasser and Scambos, 2008), Brunt (Marsh et al., 2025), Amery (Walker et al., 2021), Pine Island (Lhermitte et al., 2020; Surawy-Stepney et al., 2023b) and Thwaites (Benn et al., 2022; Surawy-Stepney et al., 2023a).

Given the critical role of surface damage in ice shelf stability, long-term and large-scale monitoring of its evolution is essential for understanding ice shelf change and reducing uncertainty in future projections. Remote sensing imagery provides
50 an important data source for such monitoring. However, publicly available surface damage products for Antarctic ice shelves remain limited (Table 1). Lai et al. (2020) produced a single-temporal surface damage map of Antarctic ice shelves for 2009 based on MODIS Mosaic of Antarctica (MOA) imagery at a spatial resolution of 125 m. Also based on MOA imagery, Pang et al. (2023) generated products for 2004, 2009 and 2014 at the same spatial resolution. Surawy-Stepney et al. (2023b) released a single-temporal product for June 2021 based on Sentinel-1 SAR imagery, at a spatial resolution of 100 m. Izeboud et al. (2025) also used SAR imagery and released products for 1997, 2000 and 2021 at a spatial resolution of 1,000 m, as
55 well as annual products for 2015–2021 at a spatial resolution of 400 m. This product represents the longest temporal coverage among existing surface damage products. The results revealed that the area of surface damage generally decreased across Antarctic ice shelves between 1997 and 2021, mainly because damaged areas were lost through calving, and that damage development was strongly correlated with ice shelf area changes (Izeboud et al., 2025). However, this product is still
60 limited by its relatively coarse spatial resolution, and continuous annual temporal coverage is only available from 2015 onwards, leaving the earlier period from 1997 through 2014 represented by only three snapshot years. More broadly, existing studies have primarily relied on MOA and SAR imagery for large-scale damage mapping. Because MOA imagery is only available for 2004, 2009 and 2014, and stable, frequent SAR acquisitions only became available after the launch of Sentinel-1 in 2014, early temporal coverage in existing products is generally sparse and discontinuous. Overall, existing openly



65 available products are limited in both spatial and temporal resolution, constraining detailed and continuous monitoring and analysis of rapidly changing ice shelves over multi-decadal time scales.

Generating long-term, high-resolution surface damage datasets requires extraction methods that are both accurate and scalable. Early studies mainly relied on manual visual interpretation of remote sensing imagery to map damage features (Hulbe et al., 2010). With the development of image processing techniques, some studies have used automatic methods such as edge detection for damage extraction (Lv et al., 2022). Izeboud and Lhermitte (2023) developed an improved image processing algorithm, the Normalised Radon Transform Detection (NeRD), and applied it to Synthetic Aperture Radar (SAR) imagery to map surface damage on Antarctic ice shelves (Izeboud et al., 2025). However, such conventional image processing methods generally rely on empirical parameter settings and may require case-specific adjustment across different regions. Deep-learning (DL) techniques, by contrast, have shown strong potential for learning representative features from remote sensing imagery (Li et al., 2024b), making them well suited to large-scale, long-term damage mapping. Related studies have applied DL methods to damage mapping using optical imagery (Lai et al., 2020; Pang et al., 2023; Zheng et al., 2024; Li et al., 2024a; Li et al., 2025b), SAR imagery (Zhao et al., 2022; Surawy-Stepney et al., 2023a; Surawy-Stepney et al., 2023b), and combined optical and SAR imagery (Huang et al., 2025). In addition to image-based mapping, altimetry data and digital elevation models (DEMs) have also been used for the identification and characterization of surface damage (Wang et al., 2021; Herzfeld et al., 2021; Li et al., 2021; Huang et al., 2024; Li et al., 2025a; Pang et al., 2026; Xu et al., 2026). However, given their limitations in spatiotemporal resolution and coverage, image-based mapping remains better suited to multi-decadal, large-scale and continuous monitoring of surface damage evolution.

To address the limitations of existing products, we apply a deep-learning method to Landsat 7/8/9 optical imagery to produce a high-resolution surface damage dataset for nine representative Antarctic ice shelves at a spatial resolution of 30 m, with multi-decadal temporal coverage from 1999 through 2024. Landsat optical imagery provides a long-term observational record that helps fill the early temporal gaps in existing SAR-based products, while also enabling higher-resolution mapping of surface damage. These nine ice shelves represent three contrasting glaciological settings and damage evolution patterns (Fig. 2). The first group comprises Pine Island, Thwaites, Crosson and Dotson in the Amundsen Sea sector, where pronounced thinning, retreat and surface damage development have been widely documented (Lilien et al., 2018; Lhermitte et al., 2020; Joughin et al., 2021; Wang et al., 2025). The second group includes Larsen B on the Antarctic Peninsula and Brunt in East Antarctica. Larsen B experienced a major collapse in 2002 and has continued to undergo further damage development, while Brunt is characterised by rift formation and recent calving events (King et al., 2018; Qiao et al., 2020; Surawy-Stepney et al., 2024; Morris et al., 2025). The third group consists of Amery, Totten and Holmes and provides additional examples from East Antarctica, including ice shelves with relatively stable conditions as well as those experiencing recent unpinning and grounding line retreat (Greene et al., 2022; Zhu et al., 2023; Miles and Bingham, 2024; Miles et al., 2025; Jin et al., 2025). Together, these ice shelves provide a representative basis for investigating long-term surface damage evolution across contrasting ice shelf settings. To extend the usable record for damage mapping, Landsat 7 scan-line-corrector-off (SLC-off) imagery acquired during 2003–2013 was first restored using a specifically designed



diffusion-model-based framework (Sect. 2.2). The dataset contains 170 surface damage maps, each representing a single ice shelf for a specific year, with temporal coverage shown in Fig. 3.

Table 1. Summary of publicly available surface damage datasets for Antarctic ice shelves (DL: deep learning, NeRD: Normalised Radon Transform Detection).

Study	Method	Sensor	Spatial Resolution	Time Span	Temporal Resolution
Lai et al. (2020)	DL	Optical	125 m	2009	Single epoch
Pang et al. (2023)	DL	Optical	125 m	2004, 2009, 2014	3 epochs
Surawy-Stepney et al. (2023b)	DL	SAR	100 m	2021	Single epoch
Izeboud et al. (2025)	NeRD	SAR	400 m 1000 m	2015–2021 1997, 2000, 2021	Annual 3 epochs
This study	DL	Optical	30 m	1999–2024	Annual

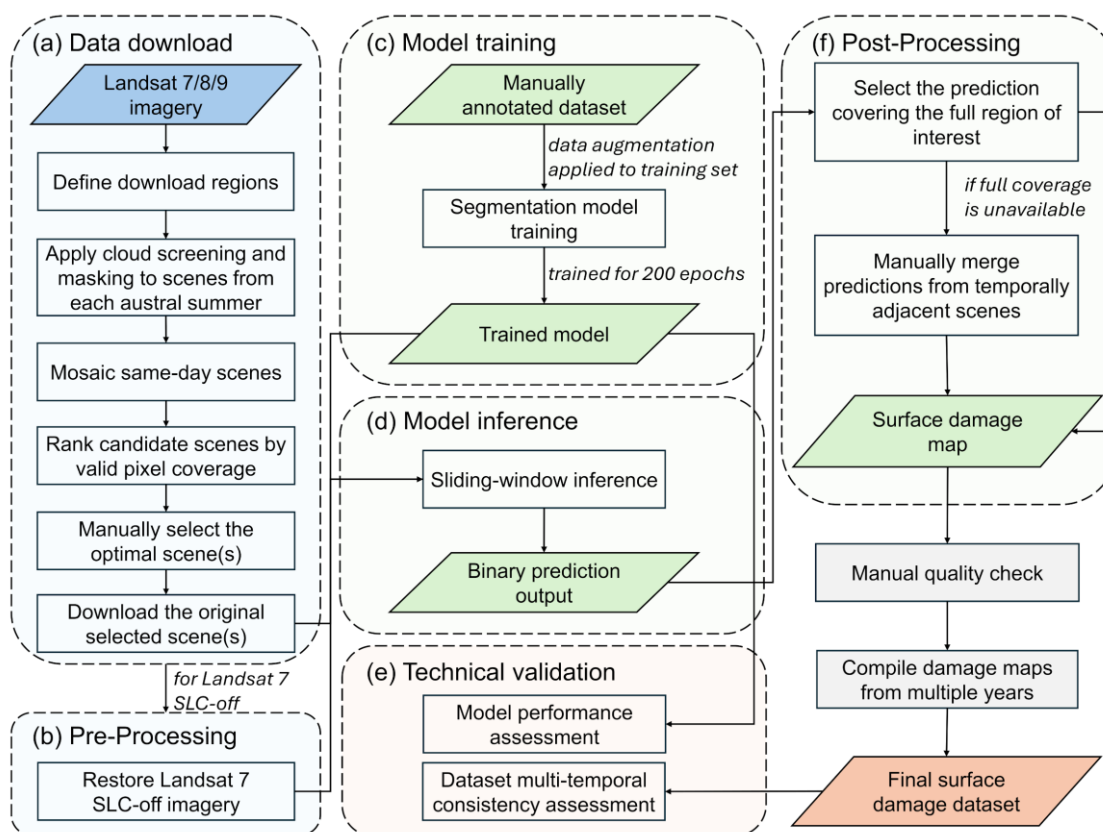
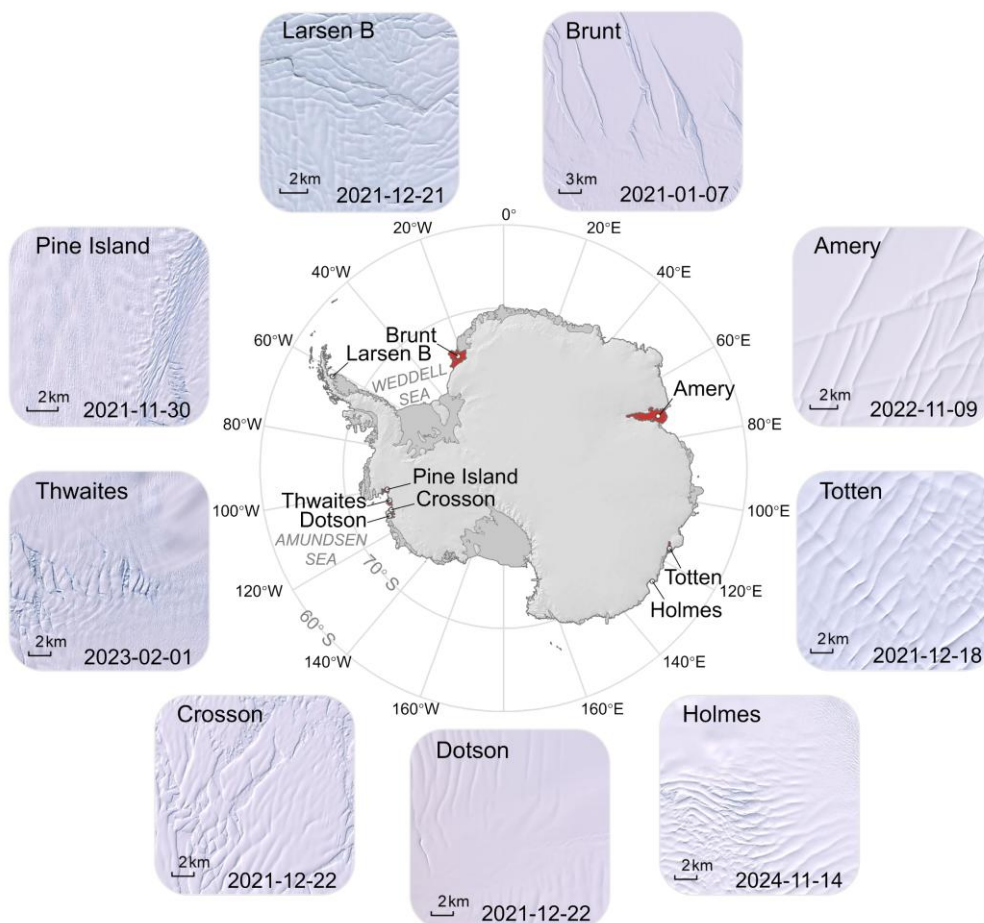


Figure 1. Workflow for surface damage mapping. Each ice shelf is processed separately. (a) Data download. (b) Pre-processing for Landsat 7 SLC-off imagery. (c) Model training. (d) Model inference. (e) Technical validation. (f) Post-processing of the dataset.



110 **Figure 2.** Spatial distribution of the nine ice shelves included in this dataset in Antarctica, with the background imagery and boundaries from Bedmap2 (Fretwell et al., 2013; Fretwell et al., 2022). Surrounding panels show representative examples of surface damage on each ice shelf, with annotations indicating the acquisition dates of the Landsat imagery.

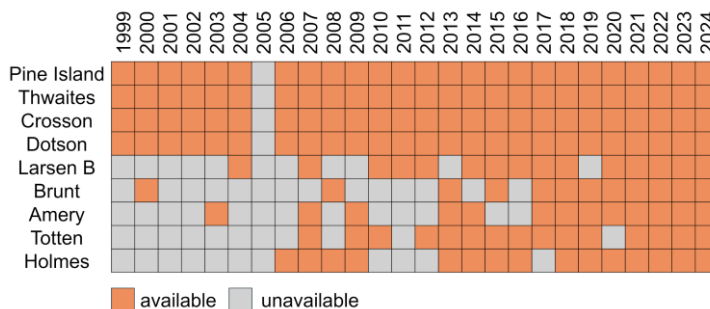


Figure 3. Temporal coverage of this dataset for each ice shelf. Orange cells denote that a surface damage map is available for that ice shelf in a given year, whereas grey cells denote that no surface damage map is available.

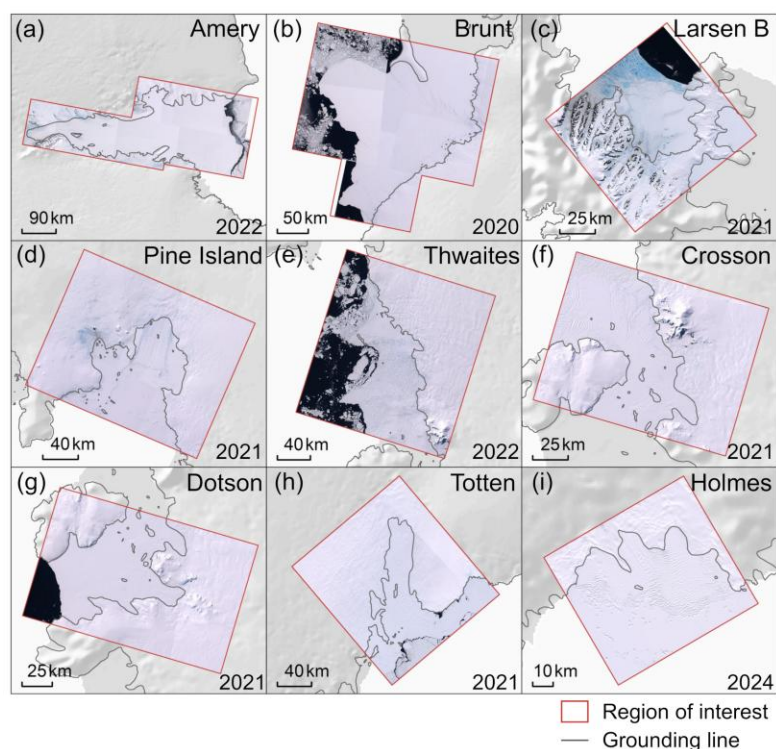


115 2 Data and methods

2.1 Regions of interest and source imagery

2.1.1 Regions of interest

During dataset generation, each ice shelf is processed separately as an independent object. To ensure sufficient coverage of the study area throughout the study period, this study determines a region of interest (ROI) for each ice shelf based on the
120 MEASUREs ice shelf extent product (Mouginot et al., 2017), combined with the maximum spatial extent of each ice shelf during the study period and with appropriate outward expansion (Fig. 4). The resulting ROI is used as the image download extent and is designed to include, as completely as possible, areas of frontal change and regions near the grounding line.



125 **Figure 4. Regions of interest (ROIs) used for imagery download and corresponding Landsat imagery for (a) Amery, (b) Brunt, (c) Larsen B, (d) Pine Island, (e) Thwaites, (f) Crosson, (g) Dotson, (h) Totten, and (i) Holmes Ice Shelves. The grounding lines are from Mouginot et al. (2017), and the annotated years indicate the austral summers from which the Landsat imagery was acquired.**

2.1.2 Data sources

To generate surface damage maps of Antarctic ice shelves for 1999–2024, this study uses optical multispectral imagery acquired by Landsat 7 (EROS Center, 2020a), Landsat 8 and Landsat 9 (EROS Center, 2020b), and selects the red, green and
130 blue (RGB) bands for processing. The imagery has a spatial resolution of 30 m (Table 2). Imagery acquired between December 1999 and March 2013 was from Landsat 7, while imagery acquired from April 2013 onwards was mainly from



135

Landsat 8, with some imagery acquired after October 2021 from Landsat 9. Owing to polar night conditions in Antarctica, the acquisition window for usable optical imagery is limited to the austral summer of each year, from November to March of the following year. In the following sections, imagery for a given year refers to imagery acquired during the corresponding austral summer.

Table 2. Data sources used for dataset generation.

Satellite	Time span	Bands	Resolution
Landsat 7	Dec 1999–Mar 2013	Red, Green, Blue (3, 2, 1)	30 m
Landsat 8	Apr 2013–Mar 2025	Red, Green, Blue (4, 3, 2)	30 m
Landsat 9	Oct 2021–Mar 2025	Red, Green, Blue (4, 3, 2)	30 m

2.1.3 Image selection and acquisition

The imagery used for dataset generation was acquired through the Google Earth Engine (GEE) platform. Landsat imagery was obtained from the Landsat Collection 2 calibrated top-of-atmosphere (TOA) reflectance dataset. Landsat imagery within the ROI of each ice shelf was screened separately for each austral summer (Fig. 1a). As cloud cover is one of the main limiting factors in the use of optical imagery in Antarctica, candidate images were first screened using a threshold of 80 % based on the ‘cloud_cover’ property in the image metadata. This threshold was set relatively loosely to retain as many potentially usable images as possible. For imagery that passed this initial screening, cloud and cloud-shadow pixels were then masked using the QA_PIXEL band provided with the Landsat products in GEE. If multiple images were available for the same day, they were mosaicked into a single daily image (hereafter referred to as a scene). The scenes were then ranked according to the proportion of valid (i.e., cloud-free) pixels, and further manually screened on this basis. Priority was given to cloud-free scenes that fully covered the ROI. If such scenes were unavailable, scenes with a relatively high proportion of valid coverage over the ROI were selected. For the final selected scenes, the original imagery without cloud masking was downloaded for subsequent dataset generation. This procedure was repeated for each ice shelf and each year from 1999 through 2024.

The downloaded imagery was exported as GeoTIFF files in unsigned 8-bit (UInt8) format. The export coordinate system was the WGS 84 / Antarctic Polar Stereographic projection (EPSG:3031), and the value range of each band was 0–255. For 2023 and 2024, some imagery exported from GEE contained large data gaps, possibly caused by anomalies during the export process. These images were instead downloaded from the USGS website (<https://earthexplorer.usgs.gov/>) as Landsat 8 Collection 2 Level-1 products. QGIS was then used for band combination, ROI clipping and data format conversion. The final output imagery was consistent with the GEE-exported imagery in format, resolution, projected coordinate system, value range and spatial extent. Through this selection and acquisition procedure, candidate scenes for damage mapping were determined for each ice shelf in each available year.



2.2 Pre-processing of Landsat 7 SLC-off imagery

160 The Landsat 7 satellite experienced a permanent failure of the scan-line corrector (SLC) in May 2003. As a result, all
imagery acquired thereafter contains stripe-shaped data gaps and is referred to as SLC-off imagery. These gaps interfere with
the extraction of surface damage on ice shelves and thus affect the mapping results. To reduce their impact, this study applies
the DiffGF framework (Tang et al., 2026b) to restore the Landsat 7 SLC-off imagery used in this study (Fig. 1b).

DiffGF is a non-reference two-stage restoration framework designed for restoring data gaps in Antarctic Landsat 7 SLC-off
165 imagery. The method first exploits the generative capability of a diffusion model to restore missing regions using only a
single SLC-off image and performs the diffusion process in latent space to improve computational efficiency. It then further
enhances the consistency between restored and known regions through a mask-guided harmonization process in pixel space,
thereby producing the final restoration result. This framework is suitable for Antarctic ice shelves that experience rapid
changes in surface conditions and effective reference imagery is difficult to obtain. Under such conditions, traditional
170 reference-based restoration methods are often difficult to apply.

The DiffGF framework was trained on SLCANT (Tang et al., 2026b), a dataset consisting of 3,139 simulated SLC-off
images of 256×256 pixels, which were generated by applying real Landsat 7 SLC-off masks to complete Landsat 8 images,
with the corresponding complete images used as ground truth. The source images were collected from 10 representative
175 regions in Antarctica, covering a range of typical Antarctic surface features, including ice- and snow-covered surfaces,
coastlines, bare rock, different types of surface damage features, blue ice and melt ponds. Further details of the construction
of this dataset and the training process of DiffGF are provided in (Tang et al., 2026b). Landsat 7 SLC-off imagery used in
this study is restored by the trained DiffGF framework, and the restored imagery is then used for damage mapping.

The restoration performance of DiffGF has also been evaluated in detail in Tang et al. (2026b) using metrics including Peak
Signal-to-Noise Ratio (PSNR) (Horé and Ziou, 2010), Universal Image Quality Index (UIQI) (Wang and Bovik, 2002),
180 Structural Similarity Index Measure (SSIM) (Wang et al., 2004), Learned Perceptual Image Patch Similarity (LPIPS) (Zhang
et al., 2018), root mean square error (RMSE) and correlation coefficient (CC).

2.3 Surface damage mapping with deep learning

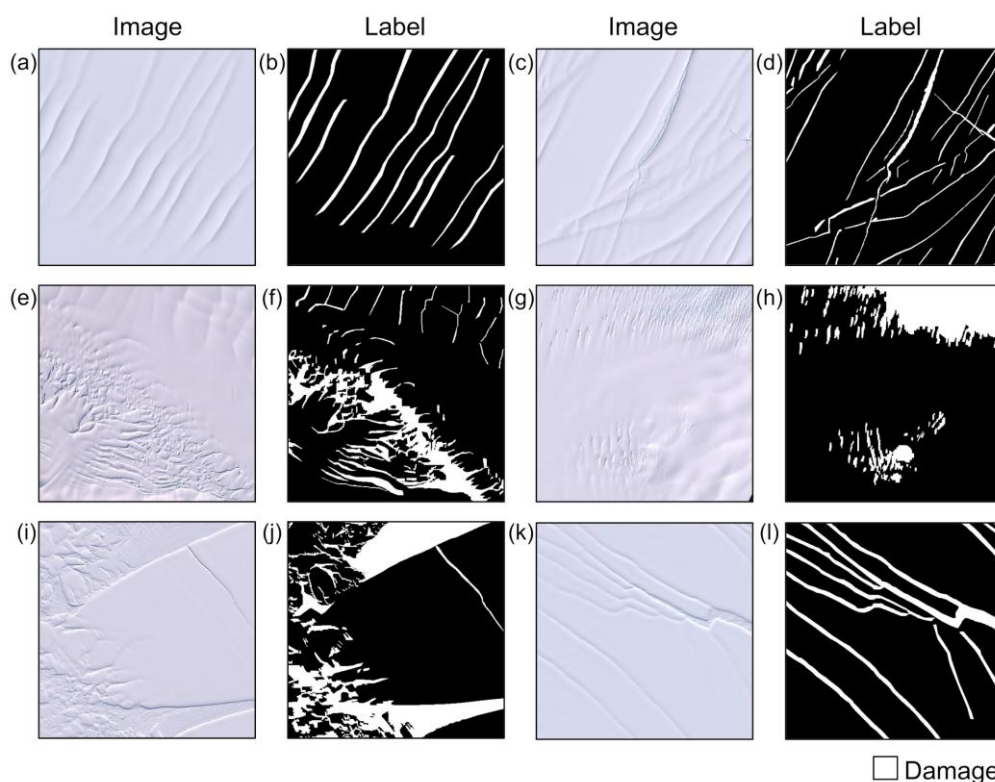
2.3.1 Manually annotated dataset

To train and test a deep-learning image segmentation model, a manually annotated surface damage dataset was created in
185 this study. The imagery used for dataset construction was selected from cloud-free Landsat 8 RGB imagery acquired over
diverse ice shelves (Fig. S1), to capture a broad range of surface damage features and help improve model robustness and
transferability. All imagery was acquired during the austral summer of 2020 (Table S1).

To improve annotation quality and confidence, the annotation process was assisted by multi-source remote sensing data,
including Sentinel-1 SAR imagery and ICESat-2 laser altimetry data acquired at similar times. This strategy allows surface
190 damage to be interpreted jointly from optical appearance, SAR backscatter characteristics, and elevation information,



helping to reduce interpretation uncertainty and subjectivity. Specifically, for each Landsat 8 image used for annotation, Sentinel-1 SAR Interferometric Wide Swath (IW) Ground Range Detected (GRD) data covering the same region and acquired close in time were downloaded and processed in SNAP through a standard workflow, including thermal noise removal, radiometric calibration, speckle filtering, and terrain correction using the REMA DEM (Howat et al., 2019; Howat et al., 2022), to derive geocoded backscatter imagery. ICESat-2 ATL06 data acquired close in time were downloaded and processed following (Wang et al., 2021) to provide additional depth information for identifying surface damage. The manually annotated dataset includes multiple types of surface damage, including crevasses, rifts, crevasse fields and heavily fractured areas, and has good sample diversity (Fig. 5). The final annotated dataset contains 276 images of 512×512 pixels.



200

Figure 5. Examples from the manually annotated surface damage dataset, showing image samples and their corresponding labels. Image samples are from Amery Ice Shelf (a and c, 2021-01-06), Crosson Ice Shelf (e, 2021-01-31), Pine Island Ice Shelf (g, 2020-12-13), Ronne Ice Shelf (i, 2021-01-15) and Larsen C Ice Shelf (k, 2020-12-29), with (b), (d), (f), (h), (j) and (l) showing the corresponding annotated labels.

205 2.3.2 Segmentation model

We used SegFormer (Xie et al., 2021) as the image segmentation model in this study. SegFormer is a Transformer-based model with the ability to capture wider spatial context, which is suitable for identifying surface damage with heterogeneous



spatial patterns and varying morphology. The model output is a binary segmentation result with two classes: damage and background.

210 2.3.3 Training strategy

The manually annotated damage dataset is used for model training and testing, with 224 images (80 %) used as the training set and 52 images (20 %) used as the test set. Images from each region are randomly allocated to the training and test sets to ensure that both subsets capture a representative range of surface damage characteristics. No spatial overlap exists between any images. To address the class imbalance between damage and background in the annotations, this study adopts a
215 composite loss function combining binary cross-entropy loss (Eq. (1)) and Dice loss (Eq. (2)), referred to as BCED (Eq. (3)), for model training:

$$\mathcal{L}_{BCE} = -\frac{1}{N} \sum_{i=1}^N [y_i \log(p_i) + (1 - y_i) \log(1 - p_i)] \quad (1)$$

$$\mathcal{L}_{Dice} = 1 - \frac{2 \sum_{i=1}^N y_i p_i + \epsilon}{\sum_{i=1}^N y_i + \sum_{i=1}^N p_i + \epsilon} \quad (2)$$

$$\mathcal{L}_{BCED} = \mathcal{L}_{BCE} + \mathcal{L}_{Dice} \quad (3)$$

220 where N denotes the total number of pixels, y_i is the ground-truth label of the i -th pixel, p_i is the probability predicted by the model that the pixel belongs to the damage class, and ϵ is a constant smoothing term.

During model training, the batch size is set to 8 and the model is trained for 200 epochs using the AdamW optimizer. For the first 20 epochs, a linear warm-up strategy is adopted to increase the learning rate from 1×10^{-5} to 1×10^{-4} . In the subsequent 80 epochs, a cosine annealing strategy is used to smoothly decay the learning rate to 5×10^{-5} . During the final 100 epochs, this
225 learning rate is maintained for final fine-tuning to promote stable model convergence. During training, random rotation and random brightness adjustment (± 25 %) are applied to the training set for data augmentation to increase sample diversity and improve model robustness and generalization ability.

2.4 Post-processing

2.4.1 Generation of full-ROI damage maps

230 The trained image segmentation model is used to map damage from the selected scenes. To generate damage maps covering the full ROI, further post-processing is carried out in this study (Fig. 1f). Because completely cloud-free optical imagery is often difficult to obtain, one final damage map is generated for each ice shelf in each year by selecting and integrating predictions from candidate scenes with the optimal spatial coverage and image quality to achieve complete ROI coverage. This strategy is based on the assumption that surface damage does not change dramatically over short time intervals, and is
235 intended to avoid fragmentation of the final product and improve the consistency of the dataset for subsequent scientific applications.



For each year, priority is given to predictions derived from a single cloud-free scene that fully covers the ROI. When more than one scene fully covers the ROI in a given year, which occurs only rarely, the prediction from one scene is selected as the final map after comparative evaluation. If no cloud-free scene can fully cover the ROI, scenes with a relatively high proportion of valid coverage and more complete coverage of rapidly flowing areas are selected first. Additional scenes that provide complementary coverage of the ROI are then selected for manual merging of the corresponding predictions. To reduce uncertainty caused by ice shelf dynamics, predictions from scenes acquired close in time are prioritized during merging.

In this study, the final merged prediction is not obtained by first mosaicking the selected scenes and then applying the segmentation model. Instead, predictions from individual selected scenes are merged directly to avoid potential interference from tonal differences at scene boundaries during damage extraction. Manual merging is guided by visual inspection of the source imagery and model predictions, with the ice velocity product (Rignot et al., 2017) used as an auxiliary reference, to ensure spatially consistent merged results and preserve local damage structures.

A complete damage map covering the ROI is then obtained for each ice shelf in each year. If complete coverage of the target ice shelf region cannot be achieved, no result is retained for that ice shelf in that year in order to maintain dataset quality. In a small number of full-ROI maps, a limited number of areas on grounded ice within the ROI but outside the main ice flow may remain affected by cloud contamination because no suitable cloud-free imagery is available for those areas. As these areas do not affect the usability of the target ice shelf region, the corresponding full-ROI maps are retained. The final maps are also manually checked against the source imagery and the results from adjacent years.

2.4.2 Product refinement to ice shelf extent

To facilitate the direct use of the dataset for scientific analysis, the full-ROI maps are further post-processed by manually defining the effective floating ice shelf extent at the corresponding time (Fig. S2). Specifically, the grounding line is fixed based on the MEaSURES ice shelf extent product (Mouginot et al., 2017), whereas the front is manually adjusted according to the corresponding imagery to exclude detached ice bodies, sea ice and other non-target areas that may affect dataset use. This process is assisted by reference products such as IceLines (Baumhoer, 2022; Baumhoer et al., 2023) and MEaSURES ITS_LIVE Antarctic Ice Sheet Extent Masks (Greene et al., 2024). It should be emphasized that these manually adjusted extents are intended only to improve product usability for ice shelf analysis and should not be interpreted as calving front mapping results.

Accordingly, two types of products are released to meet different user needs. The first type is constrained to the effective ice shelf extent, whereas the second type covers the full ROI without applying the effective extent constraint. The first type of product is subjected to strict manual inspection and is entirely derived from predictions based on high-quality cloud-free imagery. It can be used directly for scientific analysis of ice shelf surface damage. The second type of product provides more complete spatial coverage. As mentioned in Sect. 2.4.1, a small number of these full-ROI maps may contain very limited



270 areas on grounded ice outside the main ice flow that are affected by cloud or haze and require additional checking against the source imagery before use.

2.5 Technical validation methods

2.5.1 Evaluation of segmentation model performance

275 To provide a more comprehensive evaluation of the trained segmentation model, this study uses five metrics: mean intersection over union (mIoU), overall accuracy (OA), precision, recall and F1. mIoU and OA are used to assess overall segmentation performance, whereas precision, recall and F1 are calculated specifically for the damage class to evaluate the model's ability to detect surface damage.

The calculation formulae are as follows:

$$IoU = \frac{TP}{TP+FP+FN} \quad (4)$$

$$mIoU = \frac{1}{2} \sum_{i=1}^2 IoU_i \quad (5)$$

280 $OA = \frac{TP+TN}{TP+TN+FP+FN} \quad (6)$

$$Precision = \frac{TP}{TP+FP} \quad (7)$$

$$Recall = \frac{TP}{TP+FN} \quad (8)$$

$$F1 = 2 \times \frac{Precision \times Recall}{Precision + Recall} \quad (9)$$

where TP, TN, FP and FN denote true positive, true negative, false positive and false negative, respectively.

285 The same metrics are also used to assess the performance of segmentation model on DiffGF-restored Landsat 7 SLC-off imagery, by comparing the segmentation results derived from restored imagery with those derived from the corresponding original imagery.

2.5.2 Multi-temporal consistency assessment

290 As the availability of usable optical satellite imagery is affected by cloud cover, the acquisition times of the scenes used for dataset generation cannot be kept consistent across different years. In addition, the brightness and local details of optical imagery acquired at different times are affected by factors such as illumination conditions, observation geometry, the physical state of the ice shelf surface and topographic shading. Therefore, differences between damage maps of different years may reflect not only real changes in surface damage but also, in part, objective differences in the data source. To assess the influence of such source-related differences on the usability of the dataset for temporal analysis, a multi-temporal consistency assessment is carried out.

Considering that damage itself evolves dynamically, including both the formation of new damage and advection with ice flow, independent temporal tracking of all damage features is difficult to achieve. Given that damage density is an important



metric in temporal analysis and glaciological modelling, this study performs a density-based multi-temporal consistency assessment of the surface damage maps generated for each ice shelf. We assume that in most years without severe changes, such as disintegration, changes in surface damage on ice shelves are generally gradual, and therefore damage density in temporally adjacent maps should show a certain degree of correlation.

Three metrics are used for multi-temporal consistency assessment, including Spearman's rank correlation (r_s), Lin's concordance correlation coefficient (CCC, ρ_c) and root mean square error (RMSE). Among them, r_s is used to assess the consistency of the rank of pixel values in temporally adjacent damage density maps, CCC evaluates their agreement in absolute magnitude and RMSE measures their average numerical deviation. The formulae are as follows:

$$r_s = 1 - \frac{6 \sum_{i=1}^n d_i^2}{n(n^2-1)} \quad (10)$$

where n is the total number of valid pixels and d_i is the difference in relative rank of the i -th pixel between two temporally adjacent density maps.

$$\rho_c = \frac{2\sigma_{xy}}{\sigma_x^2 + \sigma_y^2 + (\mu_x - \mu_y)^2} \quad (11)$$

where μ_x and μ_y are the mean values of damage density for two temporally adjacent density maps, σ_x^2 and σ_y^2 are the variances of the two density maps, and σ_{xy} is the covariance between them.

$$RMSE = \sqrt{\frac{1}{n} \sum_{i=1}^n (x_i - y_i)^2} \quad (12)$$

where n is the total number of valid pixels and x_i and y_i are the values of the i -th pixel in two temporally adjacent density maps.

Considering the relatively rapid ice flow on ice shelves (especially for Totten, Pine Island and Thwaites), multi-temporal consistency is assessed using damage density maps calculated on a 900 m grid. For each grid cell, damage density is computed as the fraction of damage area within that cell, without resampling the original 30 m damage maps. To account for advection between adjacent time steps, the MEaSURES InSAR-based ice velocity product at 450 m resolution (Rignot et al., 2017) is used to apply a Lagrangian correction. For each temporally adjacent pair, the earlier damage density map is advected forward to the time of the later map using the ice velocity product, as follows:

$$\mathbf{x}_{t+\Delta t} = \mathbf{x}_t + \mathbf{v}(\mathbf{x}_t)\Delta t \quad (13)$$

where $\mathbf{x}_{t+\Delta t}$ is the corrected grid cell position at the time of the later map, \mathbf{x}_t is the original grid cell position in the earlier map, $\mathbf{v}(\mathbf{x}_t)$ is the ice velocity vector extracted from the ice velocity product at \mathbf{x}_t , and Δt is the time interval between adjacent maps in years.

The above metrics are then calculated by comparing the Lagrangian-corrected earlier damage density map with the original later damage density map. For comparison, the same metrics are also calculated from the original adjacent damage density maps without Lagrangian correction. Since the temporal coverage and step intervals vary across ice shelves, the median values across all adjacent pairs are used to represent the overall multi-temporal consistency.



3 Results

330 3.1 Dataset overview

The final dataset contains 170 surface damage maps at a spatial resolution of 30 m, and the temporal coverage for each ice shelf is shown in Fig. 3. Overall, temporal coverage varies among ice shelves, mainly due to the availability of optical imagery in each region. Crosson, Dotson, Pine Island and Thwaites ice shelves in the Amundsen Sea sector have relatively continuous temporal coverage during the study period, with maps available for all years except 2005. The absence of maps for 2005 is due to the lack of Landsat data acquisition during that period. Brunt and Amery ice shelves also have map series beginning earlier, in 2000 and 2003, respectively, although their early temporal coverage is not continuous. In contrast, the available maps for Larsen B, Holmes and Totten ice shelves start relatively later. The lack of early maps mainly results from the unstable acquisition quality of some early Landsat 7 imagery (e.g. overexposure), which led to a lack of usable data. However, all ice shelves maintain relatively continuous temporal coverage in the subsequent period. Representative zoomed-in examples of the surface damage maps for each ice shelf are shown in Fig. 6.

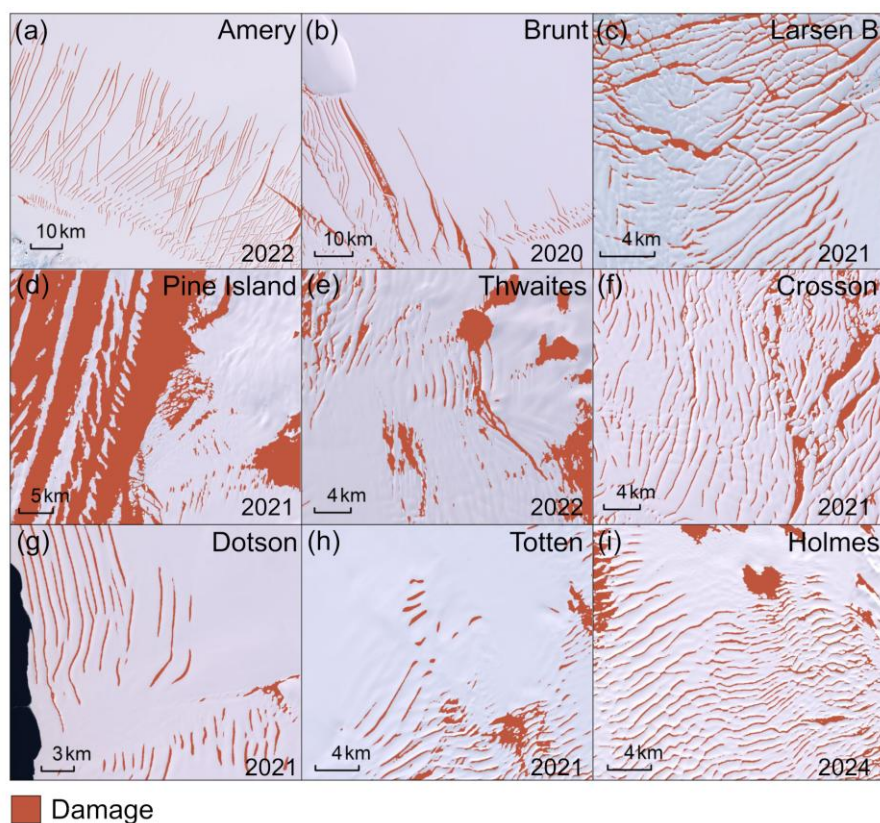


Figure 6. Zoomed-in examples of the surface damage maps for (a) Amery, (b) Brunt, (c) Larsen B, (d) Pine Island, (e) Thwaites, (f) Crosson, (g) Dotson, (h) Totten, and (i) Holmes Ice Shelves. The annotated years indicate the austral summers from which the Landsat imagery was acquired.



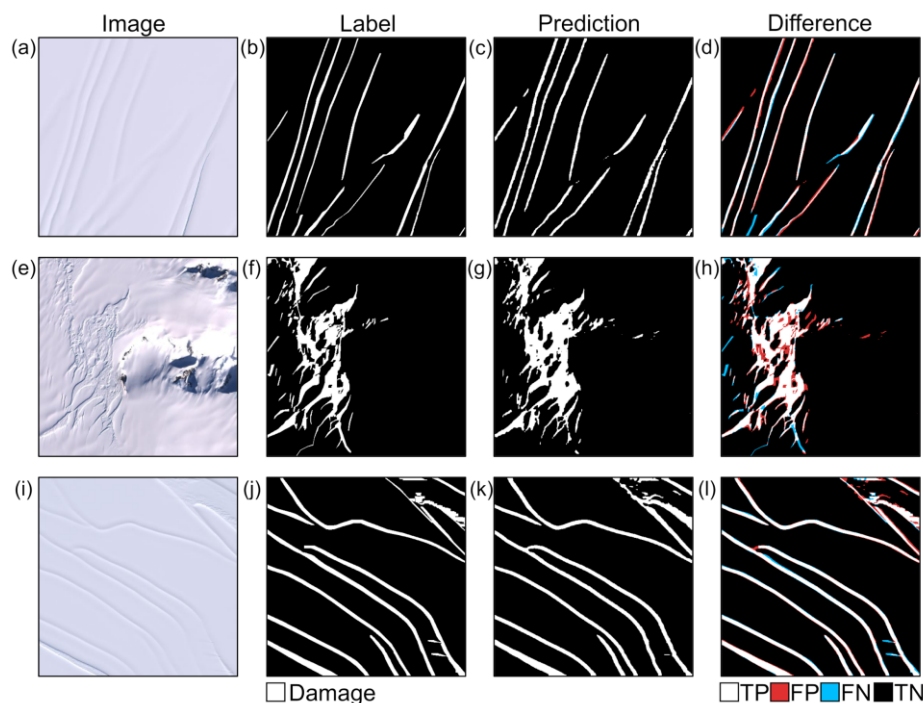
345 3.2 Dataset technical validation

3.2.1 Performance of segmentation model on the test set

The performance of the trained image segmentation model is evaluated on the test set of the manually annotated dataset. The quantitative evaluation results on the test set are presented in Table 3 and some example results are shown in Fig. 7. As shown in Fig. 7, the model predictions agree well with the manually annotated labels across three diverse test scenes, with the difference maps dominated by TP (white) pixels and only limited FP (red) and FN (blue) errors, mainly concentrated along damage boundaries. The results indicate that the model achieves good performance in surface damage extraction and is capable of identifying multiple types of surface damage with high accuracy.

Table 3. Performance of the segmentation model on the test set and an independent ice shelf (Totten Ice Shelf).

Data source	mIoU	OA	Precision	Recall	F1
Testing set	0.845	0.984	0.816	0.841	0.829
Independent ice shelf (Totten)	0.822	0.960	0.838	0.792	0.814



355

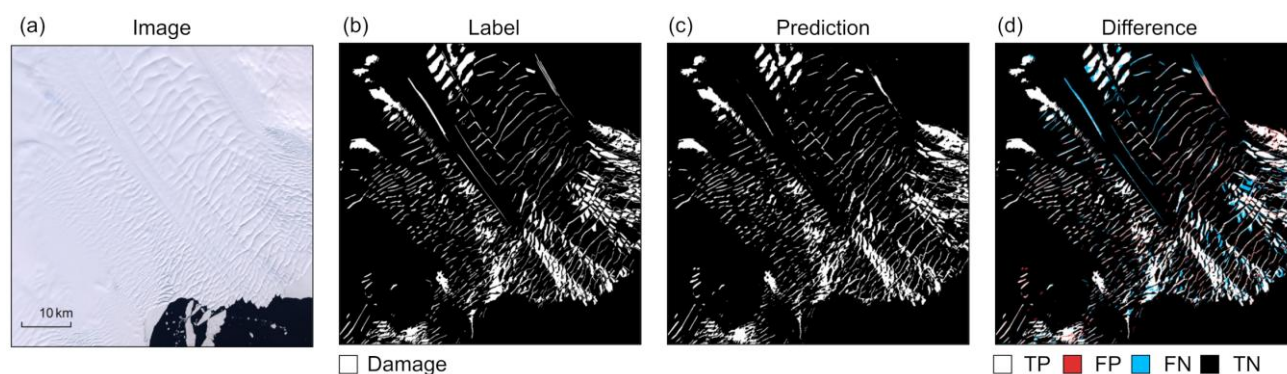
Figure 7. Examples of prediction performance on samples from the test set. (a), (e) and (i) show image samples from Amery Ice Shelf, Crosson Ice Shelf and Larsen C Ice Shelf, respectively. (b), (f) and (j) show the corresponding manually annotated labels. (c), (g) and (k) show the corresponding model predictions. (d), (h) and (l) show the pixel-wise difference maps between the corresponding labels and predictions, where TP denotes true positive, FP denotes false positive, FN denotes false negative and TN denotes true negative.

360



3.2.2 Performance of segmentation model on an independent ice shelf

To further evaluate the generalization ability of the image segmentation model, Totten Ice Shelf, which is not included in the manually annotated dataset, is selected as an independent validation site. A Landsat 8 optical image acquired on 2021-01-23 is manually annotated following the same criteria as described in Sect. 2.3.1, and the trained model is then applied to generate the prediction. As shown in Fig. 8, the prediction is overall consistent with the label, with sparse FN (blue) errors distributed along the edges of damage regions and in damage areas with relatively low image contrast. The evaluation metrics are presented in Table 3. The results indicate that the model still achieves good identification performance on an independent ice shelf that is not involved in training, demonstrating good generalization to unseen regions.



370 **Figure 8. Prediction performance on an independent ice shelf (Totten Ice Shelf).** (a) Landsat 8 image acquired on 2021-01-23. (b)
375 **Manually annotated label.** (c) Model prediction. (d) Pixel-wise difference map between label and prediction, where TP denotes
380 **true positive, FP denotes false positive, FN denotes false negative and TN denotes true negative.**

3.2.3 Performance of segmentation on restored Landsat 7 SLC-off imagery

The restoration performance of DiffGF on Landsat 7 SLC-off imagery is also evaluated (see Tang et al. (2026b)). The
375 selected area is Larsen B Ice Shelf, which contains multiple types of surface damage. This area is not included in the datasets
used for training either the DiffGF framework or the image segmentation model.

The validation imagery is constructed from a Landsat 8 image acquired on 2021-12-21, to which an SLC-off mask extracted
from a Landsat 7 SLC-off image acquired on 2012-02-20 at the same location is applied, thereby generating simulated SLC-
off imagery with ground-truth reference. DiffGF is then used to restore the simulated SLC-off imagery, and the image
380 segmentation model is applied to the restored imagery for surface damage extraction. The results are shown in Figs. 9, S3
and S4. The image quality evaluation between the restored imagery and the ground-truth imagery is shown in Table 4. The
comparison between the segmentation result from the restored imagery and that from the ground-truth imagery is shown in
Table 5.

The evaluation results indicate that DiffGF achieves good restoration performance on Landsat 7 SLC-off imagery, and that
385 the surface damage segmentation result obtained from the restored imagery (Fig. 9e) is close to that from the ground-truth



imagery (Fig. 9d). This suggests that restored Landsat 7 SLC-off imagery can serve as a reliable data source for surface damage mapping.

Table 4. Image quality metrics of the restored SLC-off test image (computed over the full image).

PSNR	UIQI	SSIM	CC	RMSE	LPIPS
35.070	0.994	0.966	0.994	0.018	0.060

Table 5. Segmentation evaluation of the restored SLC-off test image against the original complete image.

mIoU	OA	Precision	Recall	F1
0.945	0.989	0.969	0.929	0.948

390

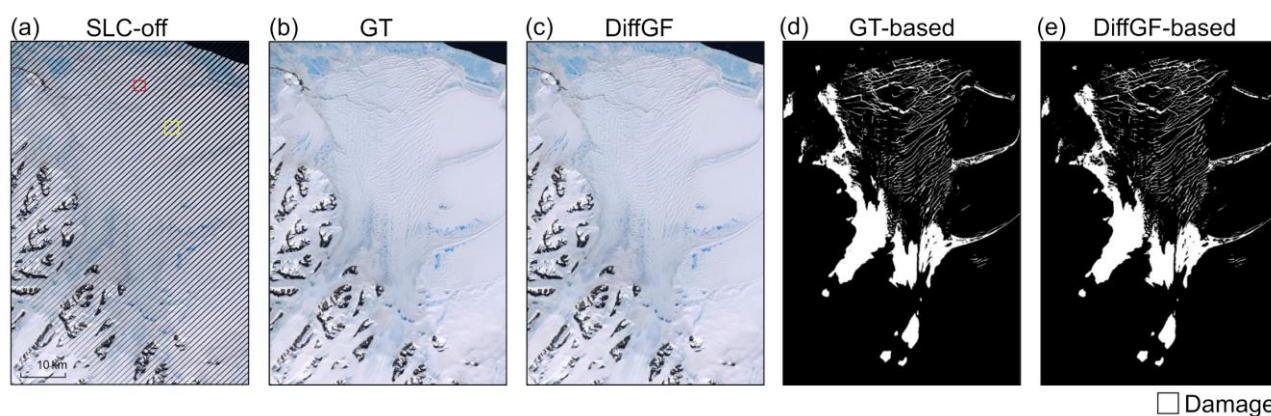


Figure 9. SLC-off restoration performance for Larsen B Ice Shelf. (a) SLC-off image with red and yellow boxes indicating zoomed-in regions shown in Figs. S3 and S4. (b) Ground truth (GT) image. (c) DiffGF-restored image. (d) Damage segmentation derived from GT. (e) Damage segmentation derived from DiffGF restoration.

395 3.2.4 Uncertainty estimation

This dataset is subject to two main sources of uncertainty: errors introduced during the segmentation process and additional uncertainty associated with damage mapping performed on DiffGF-restored Landsat 7 SLC-off imagery.

For the image segmentation model, uncertainty in damage mapping is quantified using uncertainty scaling factors derived from the model performance evaluation metrics reported in Sects. 3.2.1 and 3.2.2. From Eqs. (7) and (8), it follows that:

$$400 \quad N_{true} = \frac{Precision}{Recall} N_{pred} \quad (14)$$

Therefore, $\frac{Precision}{Recall}$ is used as the uncertainty scaling factor λ to derive uncertainty bounds for the mapped damage extent. Based on the evaluation results for the test set and the independent ice shelf (Table 3), the minimum value $\lambda_{min} = 0.971$ and the maximum value $\lambda_{max} = 1.059$ are used to define the lower and upper uncertainty bounds, respectively.

For results generated from Landsat 7 SLC-off imagery restored by DiffGF, an additional source of uncertainty arises from
 405 the restoration process itself. Given the generative nature of the diffusion model, subtle discrepancies between the restored



imagery and ground-truth surface conditions can introduce additional uncertainty into the damage mapping results. Based on the accuracy evaluation of the segmentation result from the restored imagery against that from the ground-truth imagery (Table 5), the additional scaling factor associated with DiffGF restoration is $\lambda_{DiffGF} = 1.044$. To conservatively account for this additional uncertainty, the upper uncertainty bound for results generated from DiffGF-restored imagery is further
410 adjusted to $\lambda_{max} \times \lambda_{DiffGF} = 1.105$, whereas the lower uncertainty bound remains unchanged so that the lower side of the uncertainty range is not narrowed.

These bounds should be interpreted as map-level uncertainty estimates for the mapped damage extent rather than spatially explicit pixel-wise error estimates. In addition to the uncertainty sources quantified above, the dataset is also subject to uncertainties that are more difficult to characterize. As described in Sects. 2.4.1 and 2.5.2, the final damage maps are
415 generated through a process that involves manual judgement and can also be affected by imagery acquisition conditions across years. To further assess the temporal reliability of the dataset, a multi-temporal consistency assessment is presented in the following section.

3.2.5 Multi-temporal consistency of the dataset

The multi-temporal consistency assessment results of damage density for each ice shelf are shown in Tables 6 and 7. It
420 should be noted that, for Amery Ice Shelf, the assessment is conducted separately for the entire ice shelf (full) and for the frontal region within approximately 240 km of the ice front (front). See Sect. 5 for details.

As shown in Table 6, the multi-temporal consistency of damage density in the surface damage maps is generally good for all ice shelves, with median r_s values ranging from 0.75 to 0.90, median ρ_c values ranging from 0.80 to 0.95, and median RMSE values ranging from 0.04 to 0.17. Among these ice shelves, Pine Island and Thwaites ice shelves exhibit the most
425 pronounced surface damage change over the time span of the dataset, and they also have the highest RMSE values. Compared with the results in Table 7 without Lagrangian correction based on ice velocity, the consistency metrics improve for most ice shelves after correction, as reflected by increases in r_s and ρ_c and decreases in RMSE. The improvement is most pronounced for Amery (front), Brunt and Crosson ice shelves.

For Dotson Ice Shelf, r_s decreases slightly after the Lagrangian correction is applied, indicating a small reduction in the rank-
430 order consistency of damage density values across grid cells between adjacent maps. This is mainly due to the ice flow direction near the boundary between Dotson and Crosson ice shelves (Fig. S11), where ice flows towards Crosson Ice Shelf, causing some pixels to advect beyond the original ice shelf extent after correction and thus affecting this rank-based correlation metric. In addition, ice flow on Dotson Ice Shelf is relatively slow, and the damage density maps already exhibit high temporal consistency without correction. Therefore, after correction, the exclusion of pixels near the boundary leads to
435 a slight decrease in r_s . Apart from this special case, no similar phenomenon is observed for the other ice shelves.

Overall, the dataset shows good multi-temporal consistency across temporally adjacent pairs. The improvement in consistency metrics after applying the Lagrangian correction further indicates that the temporal variations captured in the



dataset are physically consistent with ice advection, rather than arising from mapping errors. This multi-temporal consistency assessment therefore supports the reliability of the dataset for subsequent temporal analysis.

440 **Table 6. Multi-temporal consistency metrics for time-series ice shelf surface damage density after applying ice-velocity-based Lagrangian correction.**

Ice Shelf	median of τ_s	median of ρ_c	median of $RMSE$
Amery(full)	0.756	0.807	0.072
Amery(front)	0.812	0.845	0.040
Brunt	0.816	0.917	0.068
Crosson	0.884	0.913	0.074
Dotson	0.778	0.858	0.039
Holmes	0.872	0.875	0.088
Larsen B	0.887	0.950	0.091
Pine Island	0.900	0.929	0.129
Thwaites	0.846	0.862	0.173
Totten	0.893	0.860	0.067

Table 7. Multi-temporal consistency metrics for time-series ice shelf surface damage density without applying Lagrangian correction.

Ice Shelf	median of τ_s	median of ρ_c	median of $RMSE$
Amery(full)	0.680	0.723	0.094
Amery(front)	0.639	0.529	0.084
Brunt	0.626	0.812	0.112
Crosson	0.669	0.752	0.140
Dotson	0.810	0.824	0.048
Holmes	0.776	0.834	0.119
Larsen B	0.850	0.920	0.109
Pine Island	0.879	0.909	0.155
Thwaites	0.751	0.798	0.214
Totten	0.804	0.702	0.107

445 3.2.6 Comparison with existing approaches

The dataset is also compared with other existing approaches. Among the publicly available surface damage detection algorithms, only NeRD (Izeboud and Lhermitte, 2023; Izeboud et al., 2025) is applicable to the data source used in this study, and is therefore selected for comparison by processing the same optical imagery. In addition, the 100 m resolution



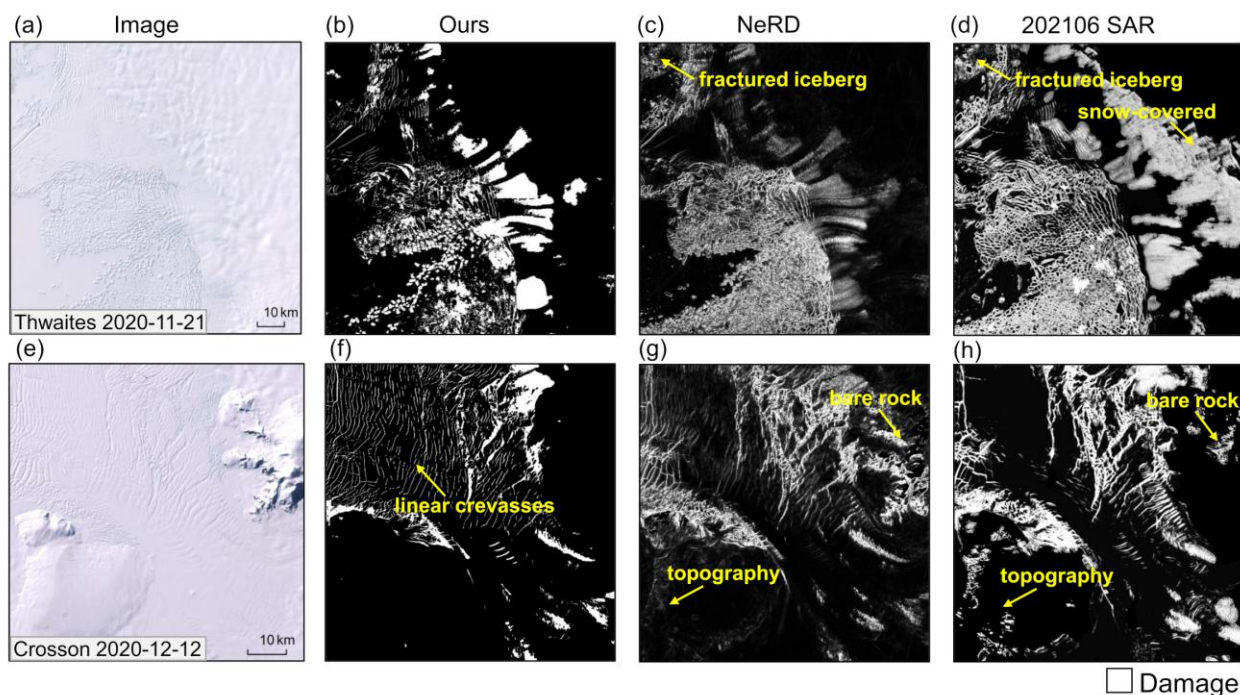
450 surface damage map of Antarctic ice shelves derived from Sentinel-1 SAR images for June 2021 by (Surawy-Stepney et al., 2023b) using a deep-learning method is also selected for comparison.

Landsat 8 optical images of Thwaites (2020-11-21) and Crosson (2020-12-12) ice shelves are selected for comparison, as they contain multiple types of surface damage features and provide a comprehensive illustration of the differences among methods and products (Fig. 10). None of the selected imagery is used in the training of the image segmentation model.

455 For the NeRD method, the official implementation provided by (Izeboud and Lhermitte, 2023) is used. A window size of 5 pixels is selected for this comparison, yielding an output spatial resolution of 150 m. Given the differing spatial resolutions across products, only qualitative comparison is performed. Our results are generally consistent with those of NeRD, showing good agreement in both the extraction of linear damage and heavily fractured areas. Furthermore, because the training dataset includes samples of features that resemble surface damage, such as edges associated with bare rock and local topography, our model successfully distinguishes true damage from structurally similar non-damage features (Fig. 10). Our
460 model also correctly excludes small fractured icebergs that are falsely identified as surface damage in the other two results. In addition, the inference speed of our deep-learning model is substantially faster than that of the image-processing-based NeRD method. For the Thwaites Ice Shelf image shown in Fig. 10a ($3,584 \times 3,584$ pixels, covering approximately $107 \text{ km} \times 107 \text{ km}$), our approach requires 22 seconds for inference, whereas NeRD requires approximately 40 minutes on the same device, representing a speedup of over $100\times$.

465 Compared with the SAR-derived surface damage map for June 2021, our results show better agreement with the SAR-based product over Thwaites Ice Shelf than over Crosson. In areas landward of the grounding line, snow-covered damage that is difficult to detect in optical imagery can be identified by SAR data owing to its penetration capability (Fig. 10d). On Crosson Ice Shelf, our method is able to identify dense linear crevasses that are absent from the SAR-based product (Fig. 10f), primarily because these features are more clearly characterized in optical imagery. Similar to the NeRD results, the SAR-
470 based product also misidentifies some edge features associated with bare rock and local topography as damage (Fig. 10h). Such misclassification may be related to the training strategy of Surawy-Stepney et al. (2023b), where the model was initially trained on manually annotated calving fronts and may therefore be more sensitive to linear features. The limited spectral information available from single-band SAR data may further increase the difficulty in distinguishing surface damage from edge features with similar backscatter responses. Nevertheless, such misclassification can be mitigated through
475 post-processing using a bare rock dataset and an ice shelf extent mask.

Overall, our results show high consistency with those of NeRD (Izeboud and Lhermitte, 2023) when using the same optical data source, while providing higher spatial resolution and substantially improved computational efficiency. Compared with the SAR-based results of Surawy-Stepney et al. (2023b), our results show good agreement for damage features visible in
480 both data sources, and also provide higher spatial resolution. Compared with existing approaches, the deep-learning-based method used in this study achieves good extraction performance with high computational efficiency, making it well suited to large-area, long-term dataset production. In addition, the use of Landsat RGB imagery in this study enables richer spectral characterization of surface damage and makes it possible to extend the time-series mapping back to 1999.



485 **Figure 10.** Comparison of the generated dataset with existing approaches. (a) and (e) show optical images of Thwaites Ice Shelf and Crosson Ice Shelf, respectively. (b) and (f) show the results of this dataset. (c) and (g) show the results generated by NeRD (Izeboud and Lhermitte, 2023). (d) and (h) show the released SAR-based map for June 2021 (Surawy-Stepney et al., 2023b). The results of this dataset are displayed as binary values of 0 and 1, whereas the NeRD and SAR-based results for June 2021 are displayed in the range [0,1] with standard deviation stretch applied to enhance visual clarity.

490 3.3 Time-series characteristics of surface damage

To characterize the temporal variation in surface damage development for each ice shelf over the study period, surface damage area and surface damage fraction are calculated for each map. The formula for calculating damage fraction is as follows:

$$495 \text{ damage fraction} = \frac{\text{damage area}}{\text{ice shelf area}} \quad (15)$$

where ice shelf area is the area of the manually delineated ice shelf extent for the corresponding period. Readers may also calculate the corresponding damage fraction using their own customized ice shelf extent.

The temporal variations of surface damage fraction and area are shown in Fig. 11, with shaded regions indicating the uncertainty bounds estimated in Sect. 3.2.4. For the damage fraction, uncertainty in the ice shelf area was not included in these shaded bounds. Overall, the nine ice shelves can be broadly grouped into two categories based on the magnitude of temporal change in surface damage. The first category includes Pine Island, Thwaites and Larsen B ice shelves, which show relatively large changes in surface damage fraction during the study period (Figs. 11a and 12–14). The remaining ice shelves



fall into the second category, where surface damage shows less pronounced temporal change during this period (Figs. 15, S7 and S9–S13).

Among the ice shelves with more pronounced surface damage change, Pine Island (Fig. 12) and Larsen B (Fig. 14) show clear development of new damage, with the ice shelf surface becoming progressively more damaged along the main ice flow direction and in shear margin areas. These patterns are consistent with the documented accelerated flow and instability of these ice shelves (Lhermitte et al., 2020; Joughin et al., 2021; Qiao et al., 2020; Ochwat et al., 2024). Thwaites also shows pronounced changes (Fig. 13). Thwaites West Ice Tongue (TWIT) undergoes intense fragmentation and disintegration during the study period, whereas surface damage continues to increase on Thwaites East Ice Shelf (TEIS). These changes are in line with the reported structural weakening of Thwaites Ice Shelf (Benn et al., 2022; Wang et al., 2025). For further analysis of Thwaites, readers are advised to use the full-ROI damage maps, which have a larger effective data domain, for customized analysis.

Among the ice shelves with less pronounced surface damage change, the results still capture the evolution of surface damage and changes associated with calving. These characteristics are reflected in the mapped spatial distribution of damage and the temporal variations (e.g., Amery Ice Shelf, Figs. S7 and S9, and Holmes Ice Shelf, Fig. S12). Brunt Ice Shelf has a larger overall area than other ice shelves in this dataset, so even though calving events occur during the study period, the resulting changes in damage fraction and area are relatively modest. Nevertheless, the results capture increased damage within the shear margin areas and clearly reflect the morphology of rifts prior to calving (Fig. 15).

These example analyses demonstrate that this dataset can characterize the temporal evolution of surface damage on ice shelves and the details of specific change events, thereby contributing to the understanding of ice shelf dynamics.

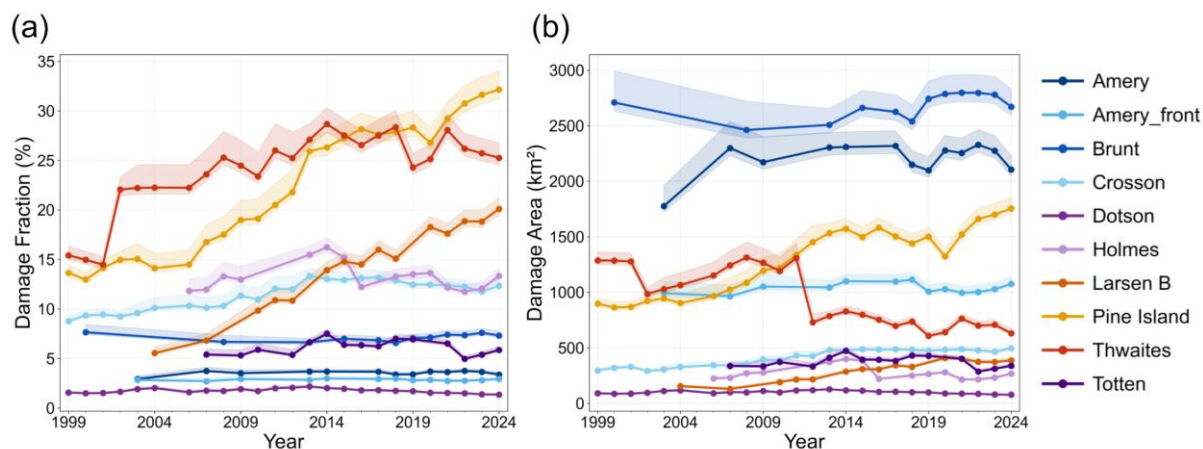
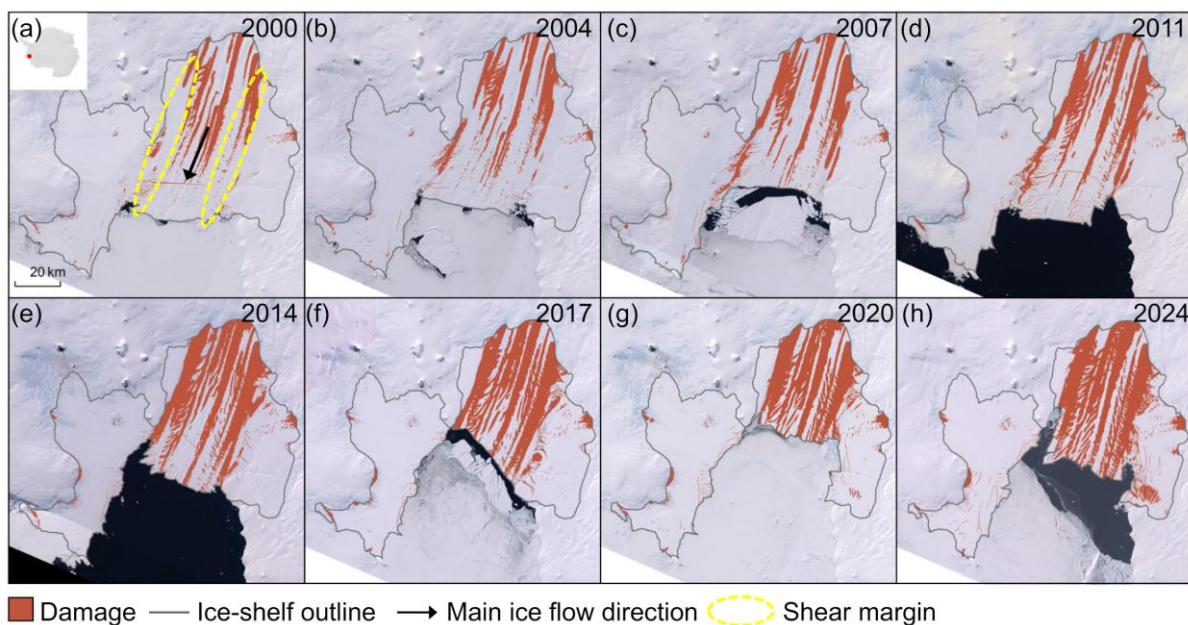


Figure 11. Temporal variations in damage fraction (a) and damage area (b) for the ice shelves in the dataset during 1999–2024. Colour-vision-deficiency-friendly versions of this figure are provided in Figs. S5 and S6.



525 **Figure 12.** Representative surface damage maps of Pine Island Ice Shelf for (a) 2000, (b) 2004, (c) 2007, (d) 2011, (e) 2014, (f) 2017, (g) 2020 and (h) 2024. The location of Pine Island Ice Shelf in Antarctica is shown in (a).

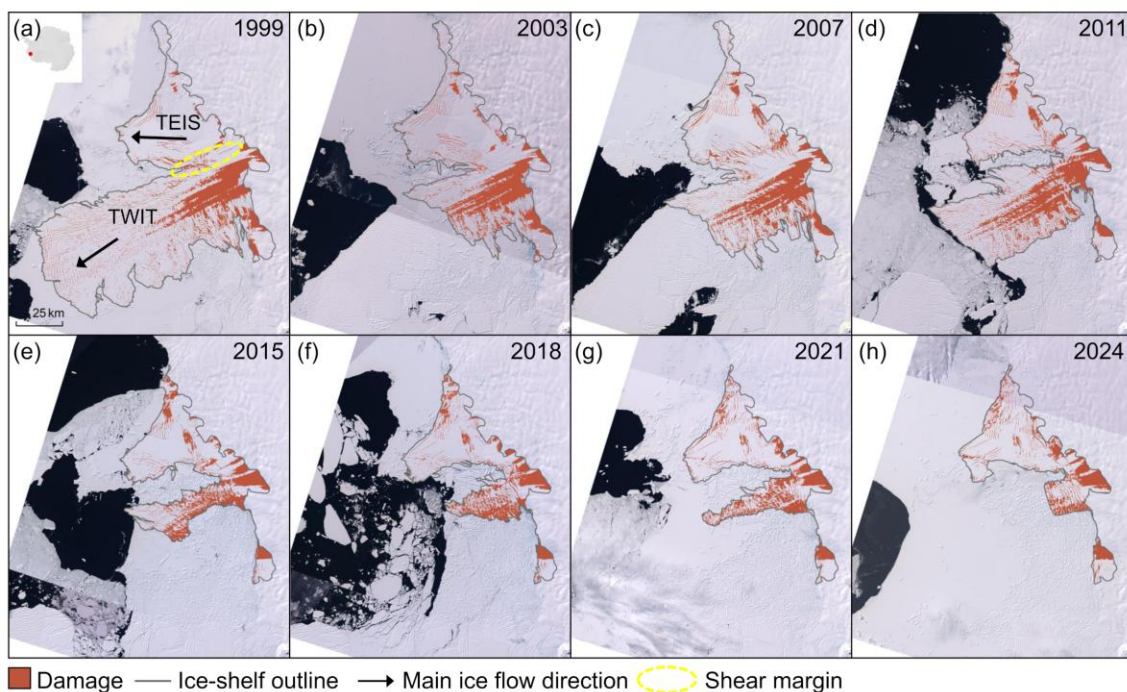
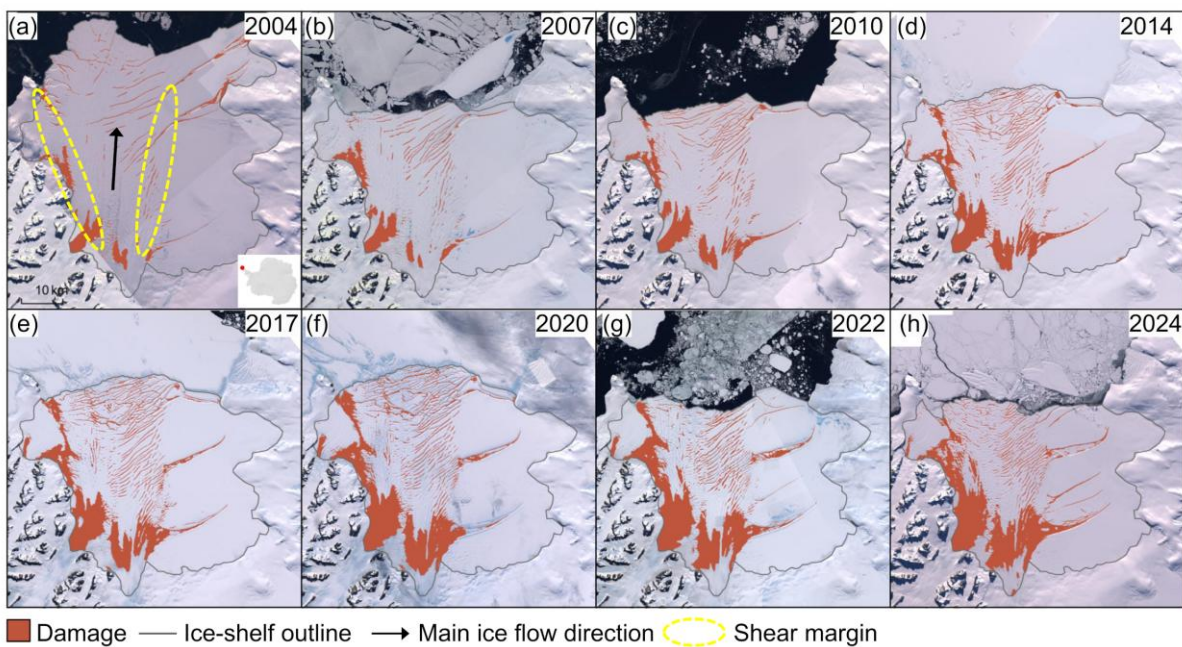
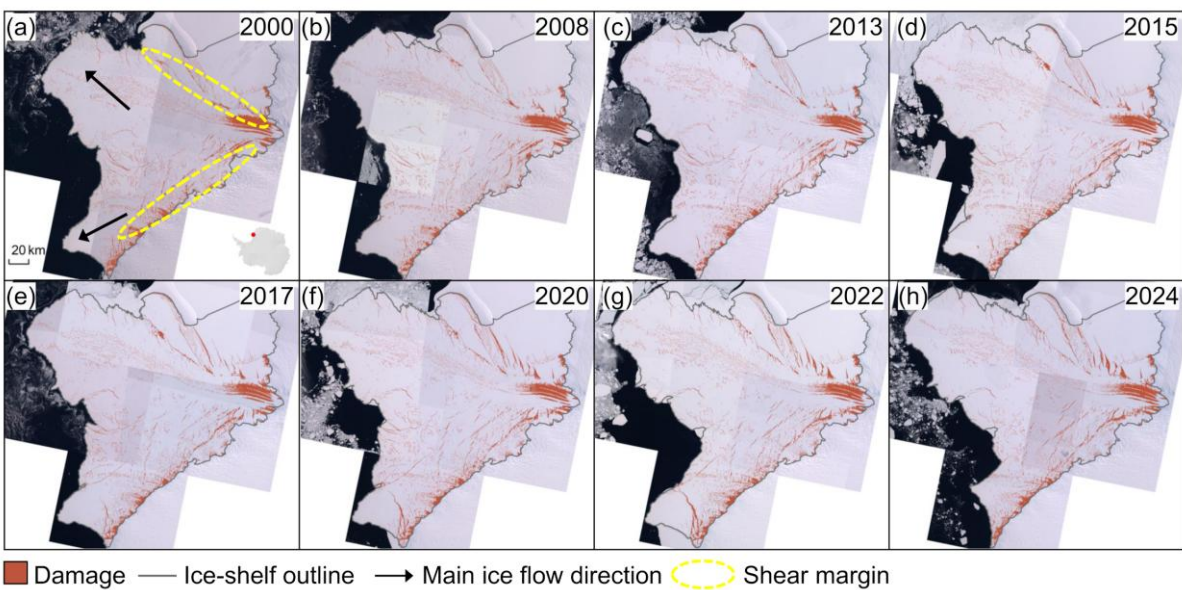


Figure 13. Representative surface damage maps of Thwaites Ice Shelf for (a) 1999, (b) 2003, (c) 2007, (d) 2011, (e) 2015, (f) 2018, (g) 2020 and (h) 2024. The location of Thwaites Ice Shelf in Antarctica is shown in (a).



530

Figure 14. Representative surface damage maps of Larsen B Ice Shelf for (a) 2004, (b) 2007, (c) 2010, (d) 2014, (e) 2017, (f) 2020, (g) 2022 and (h) 2024. The location of Larsen B Ice Shelf in Antarctica is shown in (a).



535

Figure 15. Representative surface damage maps of Brunt Ice Shelf for (a) 2000, (b) 2008, (c) 2013, (d) 2015, (e) 2017, (f) 2020, (g) 2022 and (h) 2024. The location of Brunt Ice Shelf in Antarctica is shown in (a).



4 Usage notes

In the released dataset, each ice shelf is stored in a separate folder, and within each folder a subfolder is provided for each available year. An example path is:

[Ice_Shelf_Name]/[YYYY]

540 Each yearly subfolder stores the surface damage maps for the corresponding ice shelf and year. According to the two product types defined in Sect. 2.4.2, each yearly subfolder contains two types of product files.

The first type of product file is named:

[Sensor]_[Ice_Shelf_Name]_[YYYY](_slc_off_DiffGF)_damage_map.tif

The second type of product file is named:

545 [Sensor]_[Ice_Shelf_Name]_[YYYY](_slc_off_DiffGF)_damage.tif

In the [Sensor] field, ‘LE07’, ‘LC08’ and ‘LC09’ indicate that the result is derived from Landsat 7, Landsat 8 and Landsat 9 imagery, respectively. If the filename contains more than one [Sensor] value, this indicates that the result was derived from imagery acquired by more than one satellite. If the filename contains ‘_slc_off_DiffGF’, this indicates that the corresponding data source is DiffGF-restored Landsat 7 SLC-off imagery.

550 All GeoTIFF files are internally compressed using LZW compression and stored as single-band unsigned 8-bit integer (UInt8) raster files at 30 m spatial resolution in the WGS 84 / Antarctic Polar Stereographic projection (EPSG:3031). The first type includes only the results within the effective ice shelf extent, where 0 indicates background, 1 indicates damage, and areas outside the effective extent are set to NoData (255). The second type includes results for the full ROI, where 0 indicates background and 255 indicates damage, without applying the effective extent constraint.

555 As described in Sect. 2.4.2, the second type of product requires additional manual checking against the corresponding source imagery before use.

In addition, the root folder includes a metadata.ods file recording the acquisition dates of the imagery used to generate the results. The ROIs used for imagery download are provided as GeoPackage files.

5 Discussion

560 This dataset provides a high-resolution long-term record of surface damage mapping for ice shelves since 1999 and offers new insights into Antarctic ice shelf stability. Compared with products at the 1 km scale that identify whether damage signals are present within each pixel (Izeboud et al., 2025), this dataset has a higher spatial resolution of 30 m, enabling better preservation of the morphological characteristics of damage features. At 1 km resolution, surface damage is significantly aggregated and finer damage features remain undetected, which may obscure the early-stage damage
565 development. Our dataset therefore supports more detailed temporal analysis of damage evolution at finer spatial scales. Previous studies have shown that incorporating damage evolution into numerical ice flow models can substantially enhance ice flow acceleration and mass loss, but large uncertainties remain in the associated parameters (Ranganathan et al., 2025).



The high-resolution time-series surface damage maps provided by this dataset document the spatial distribution and temporal evolution of observable surface damage, and can be used to improve the damage representation and parameterization in numerical models that incorporate damage mechanisms.

To generate observations over a long time span with high temporal continuity, Landsat optical imagery is used as the data source in this study for the period 1999–2024 considering public availability, spatial resolution and temporal consistency. The availability of optical imagery is limited by cloud cover, and usable imagery can only be acquired during the austral summer in Antarctica. As surface damage generally evolves gradually over annual time scales, this is not considered a major limitation because this study is dedicated to characterizing long-term damage evolution. Optical imagery acquired at different times varies in imaging conditions such as illumination angle. For ice shelf areas, the overall influence on damage mapping is relatively limited. However, for grounded ice areas, where surface damage is generally shallower, damage extraction is more easily affected by these variations. These areas are not included in the first type of product, and results from the second type of product (full-ROI) in such regions should therefore be interpreted with caution.

Although the 30 m resolution of Landsat imagery is relatively high among openly available multi-decadal Earth observation datasets, it remains challenging at this scale to distinguish densely distributed damage features individually. This phenomenon is especially pronounced in regions such as the Pine Island ice tongue, where continuous and densely clustered surface damage often appears in Landsat imagery as contiguous rough-textured areas (Fig. 12). As shown in Fig. S14, airborne high-resolution images (Operation IceBridge CAMBOT L1B Geolocated Images, 10 cm resolution; Studinger and Harbeck, 2019), together with triangulated irregular network (TIN) examples derived from airborne altimetry data (Operation IceBridge ATM L1B Elevation and Return Strength; Studinger, 2013), indicate that such contiguous areas in Landsat imagery correspond to actual linear damage features and surface depressions. On this basis, for densely clustered damage features that cannot be reliably separated from each other at 30 m resolution, this study adopts a connected-region annotation strategy (Fig. 5h). In addition, different types of surface damage are not distinguished in this dataset, and surface expressions caused by basal crevasses may also be included in the maps. As a result, more detailed differentiation of damage types requires evidence from other data sources. Future work could further develop classification mapping of damage types.

Among the ice shelves included in the dataset, Amery Ice Shelf is strongly affected by surface meltwater, especially in the area near the southern grounding line, where both seasonal and interannual variations in surface meltwater and stream networks (Surawy-Stepney et al., 2023b; Spergel et al., 2021) can interfere with damage extraction (Fig. S7 and S8). This also contributes to the apparent increase in damage area for Amery Ice Shelf during 2003–2007 (Fig. 11b). A subregional product covering the frontal ~240 km of the ice shelf (Amery_front) is therefore also released, and it shows a more stable representation of damage evolution near the calving front (Fig. S9 and Tables 6 and 7). No similar influence is evident for the other ice shelves included in the dataset.

The generation of this dataset relies on cloud-free optical imagery and, for many results, requires manual merging of predictions from multiple scenes to obtain damage maps with complete ROI coverage. Consequently, the current dataset is



limited to nine representative ice shelves. In the future, the processing workflow developed in this study can be applied to other Antarctic ice shelves to achieve Antarctic-wide, long-term mapping of surface damage on ice shelves.

6 Code and data availability

The code used in this study, including the Google Earth Engine scripts for Landsat image acquisition, the surface damage mapping inference code, and the scripts for generating the temporal variation analysis shown in Fig. 11, is available at <https://github.com/tly-code/surface-damage-seg>. The code for the DiffGF framework is available at <https://github.com/tly-code/DiffGF>. The surface damage dataset generated in this study is available from Zenodo at <https://doi.org/10.5281/zenodo.20425951> (Tang et al., 2026a, v1).

7 Conclusions

This study produces a long-term surface damage dataset for nine representative Antarctic ice shelves based on Landsat optical imagery for the period 1999–2024. The dataset contains 170 maps at a spatial resolution of 30 m. During dataset generation, a deep-learning image segmentation model is used for automatic extraction of surface damage. For Landsat 7 SLC-off imagery used during 2003–2013, pre-processing is carried out using a diffusion-model-based non-reference restoration framework.

Validation results from the test set and an independent ice shelf indicate that the image segmentation model used in this study has good performance in extracting surface damage. Validation of Landsat 7 SLC-off imagery restored by DiffGF shows that it can serve as a reliable data source for mapping in this dataset. Qualitative comparison with the NeRD method (Izeboud and Lhermitte, 2023) and a SAR-based product (Surawy-Stepney et al., 2023b) shows that the results of this dataset are generally consistent with existing approaches, while providing higher spatial resolution and temporal continuity compared to currently available long-term products.

The dataset shows that, among the nine ice shelves studied, Pine Island, Thwaites and Larsen B ice shelves experience the most pronounced changes in surface damage during 1999–2024. Surface damage on Pine Island and Larsen B ice shelves continues to increase, while Thwaites Ice Shelf shows both significant disintegration processes and surface damage evolution over the same period. Brunt Ice Shelf also shows increased damage in the shear margin areas, whereas the remaining ice shelves remain relatively stable during the study period. The dataset and results presented in this study offer new insights into the temporal evolution of surface damage on Antarctic ice shelves and can help improve current understanding of Antarctic Ice Sheet instability.



Author contributions

Contributions are according to CRediT. Conceptualization: LT and JLB. Data curation: LT. Formal analysis: LT, JLB and
630 TL. Methodology: LT and JLB. Software: LT. Supervision: JLB and GQ. Validation: LT, JLB, TL and GQ. Visualization:
LT and TL. Writing (original draft): LT. Writing (review and editing): LT, JLB, TL and GQ.

Competing interests

The contact author has declared that none of the authors has any competing interests.

Disclaimer

635 Publisher's note: Copernicus Publications remains neutral with regard to jurisdictional claims made in the text, published
maps, institutional affiliations, or any other geographical representation in this paper. While Copernicus Publications makes
every effort to include appropriate place names, the final responsibility lies with the authors. Views expressed in the text are
those of the authors and do not necessarily reflect the views of the publisher.

Acknowledgements

640 This work was carried out using the computational facilities of the Advanced Computing Research Centre, University of
Bristol - <http://www.bristol.ac.uk/acrc/>.

We thank the USGS for providing the Landsat 7/8/9 imagery.

During the preparation of this manuscript, ChatGPT was used in order to enhance the readability. After using this tool, the
authors reviewed and edited the content as needed and take full responsibility for the content of the publication.

645 Financial support

This work is supported by the National Natural Science Foundation of China (42276249, 42394131), the Science and
Technology Commission of Shanghai Municipality(23230712200), and the Fundamental Research Funds for the Central
Universities.

Tian Li is funded by the Leverhulme Early Career Fellowship (ECF-2024-157).



650 References

- Bassis, J., Crawford, A., Kachuck, S., Benn, D., Walker, C., Millstein, J., Duddu, R., Åström, J., Fricker, H., and Luckman, A.: Stability of Ice Shelves and Ice Cliffs in a Changing Climate, *Annual Review of Earth and Planetary Sciences*, 52, 221–247, <https://doi.org/10.1146/annurev-earth-040522-122817>, 2024.
- Baumhoer, C.: IceLines - Sentinel-1 - Antarctica, German Aerospace Center (DLR) [data set],
655 <https://doi.org/10.15489/BTC4QU75GR92>, 2022.
- Baumhoer, C. A., Dietz, A. J., Heidler, K., and Kuenzer, C.: IceLines – A new data set of Antarctic ice shelf front positions, *Scientific Data*, 10, 138, <https://doi.org/10.1038/s41597-023-02045-x>, 2023.
- Benn, D., Luckman, A., Åström, J., Crawford, A., Cornford, S., Bevan, S., Zwinger, T., Gladstone, R., Alley, K., Pettit, E.,
660 and Bassis, J.: Rapid fragmentation of Thwaites Eastern Ice Shelf, *Cryosphere*, 16, 2545–2564, <https://doi.org/10.5194/tc-16-2545-2022>, 2022.
- Borstad, C., Khazendar, A., Larour, E., Morlighem, M., Rignot, E., Schodlok, M., and Seroussi, H.: A damage mechanics assessment of the Larsen B ice shelf prior to collapse: Toward a physically-based calving law, *Geophysical Research Letters*, 39, L18502, <https://doi.org/10.1029/2012gl053317>, 2012.
- Colgan, W., Rajaram, H., Abdalati, W., McCutchan, C., Mottram, R., Moussavi, M., and Grigsby, S.: Glacier crevasses:
665 Observations, models, and mass balance implications, *Reviews of Geophysics*, 54, 119–161, <https://doi.org/10.1002/2015rg000504>, 2016.
- Davison, B., Hogg, A., Gourmelen, N., Jakob, L., Wuite, J., Nagler, T., Greene, C., Andreasen, J., and Engdahl, M.: Annual mass budget of Antarctic ice shelves from 1997 to 2021, *Science Advances*, 9, eadi0186, <https://doi.org/10.1126/sciadv.adi0186>, 2023.
- 670 Earth Resources Observation and Science (EROS) Center: Landsat 7 Enhanced Thematic Mapper Plus Level-1, Collection 2, U.S. Geological Survey [data set], <https://doi.org/10.5066/P9TU80IG>, 2020a.
- Earth Resources Observation and Science (EROS) Center: Landsat 8-9 Operational Land Imager / Thermal Infrared Sensor Level-1, Collection 2, U.S. Geological Survey [data set], <https://doi.org/10.5066/P975CC9B>, 2020b.
- Fretwell, P., Pritchard, H., Vaughan, D., Bamber, J., Barrand, N., Bell, R., Bianchi, C., Bingham, R., Blankenship, D.,
675 Casassa, G., Catania, G., Callens, D., Conway, H., Cook, A., Corr, H., Damaske, D., Damm, V., Ferraccioli, F., Forsberg, R., Fujita, S., Gim, Y., Gogineni, P., Griggs, J., Hindmarsh, R., Holmlund, P., Holt, J., Jacobel, R., Jenkins, A., Jokat, W., Jordan, T., King, E., Kohler, J., Krabill, W., Riger-Kusk, M., Langley, K., Leitchenkov, G., Leuschen, C., Luyendyk, B., Matsuoka, K., Mouginot, J., Nitsche, F., Nogi, Y., Nost, O., Popov, S., Rignot, E., Rippin, D., Rivera, A., Roberts, J., Ross, N., Siegert, M., Smith, A., Steinhage, D., Studinger, M., Sun, B., Tinto, B., Welch, B., Wilson, D., Young, D., Xiangbin, C.,
680 and Zirizzotti, A.: Bedmap2: improved ice bed, surface and thickness datasets for Antarctica, *Cryosphere*, 7, 375–393, <https://doi.org/10.5194/tc-7-375-2013>, 2013.



- Fretwell, P., Fremand, A., Bodart, J., Pritchard, H., Vaughan, D., Bamber, J., Barrand, N., Bell, R. E., Bianchi, C., Bingham, R., Blankenship, D., Casassa, G., Catania, G., Callens, D., Conway, H., Cook, A., Corr, H., Damaske, D., Damn, V., Ferraccioli, F., Forsberg, R., Fujita, S., Gim, Y., Gogineni, P., Griggs, J., Hindmarsh, R., Holmlund, P., Holt, J. W., Jacobel, R., Jenkins, A., Jokat, W., Jordan, T., King, E., Kohler, J., Krabill, W., Riger-Kusk, M., Langley, K., Leitchenkov, G., Leuschen, C., Luyendyk, B., Matsuoka, K., Mouginot, J., Nitsche, F., Nogi, Y., Nost, O., Popov, S., Rignot, E., Rippin, D., Rivera, A., Roberts, J. L., Ross, N., Siegert, M., Smith, A., Steinhage, D., Studinger, M., Sun, B., Tinto, K., Welch, B., Wilson, D. S., Young, D., Xiangbin, C., and Zirizzotti, A.: BEDMAP2 - Ice thickness, bed and surface elevation for Antarctica - standardised data points, NERC EDS UK Polar Data Centre [data set], <https://doi.org/10.5285/2FD95199-365E-4DA1-AE26-3B6D48B3E6AC>, 2022.
- Fricker, H. A., Galton-Fenzi, B. K., Walker, C. C., Freer, B. I. D., Padman, L., and DeConto, R.: Antarctica in 2025: Drivers of deep uncertainty in projected ice loss, *Science*, 387, 601–609, <https://doi.org/10.1126/science.adt9619>, 2025.
- Glasser, N. and Scambos, T.: A structural glaciological analysis of the 2002 Larsen B ice-shelf collapse, *Journal of Glaciology*, 54, 3–16, <https://doi.org/10.3189/002214308784409017>, 2008.
- Greene, C. A., Gardner, A. S., Schlegel, N.-J., and Fraser, A. D.: Antarctic calving loss rivals ice-shelf thinning, *Nature*, 609, 948–953, <https://doi.org/10.1038/s41586-022-05037-w>, 2022.
- Greene, C. A., Gardner, A. S., Schlegel, N., and Fraser, A. D.: MEaSURES ITS_LIVE Antarctic Annual 240 m Ice Sheet Extent Masks, 1997–2021, Version 1, NASA National Snow and Ice Data Center Distributed Active Archive Center [data set], <https://doi.org/10.5067/9ZFX84T5GI6D>, 2024.
- Herzfeld, U., Trantow, T., Lawson, M., Hans, J., and Medley, G.: Surface heights and crevasse morphologies of surging and fast-moving glaciers from ICESat-2 laser altimeter data - Application of the density-dimension algorithm (DDA-ice) and evaluation using airborne altimeter and Planet SkySat data, *Science of Remote Sensing*, 3, 100013, <https://doi.org/10.1016/j.srs.2020.100013>, 2021.
- Horé, A. and Ziou, D.: Image Quality Metrics: PSNR vs. SSIM, 2010 20th International Conference on Pattern Recognition, 2366–2369, <https://doi.org/10.1109/ICPR.2010.579>, 2010.
- Howat, I., Porter, C., Smith, B., Noh, M., and Morin, P.: The Reference Elevation Model of Antarctica, *Cryosphere*, 13, 665–674, <https://doi.org/10.5194/tc-13-665-2019>, 2019.
- Howat, I., Porter, C., Noh, M.-J., Husby, E., Khuvis, S., Danish, E., Tomko, K., Gardiner, J., Negrete, A., Yadav, B., Klassen, J., Kelleher, C., Cloutier, M., Bakker, J., Enos, J., Arnold, G., Bauer, G., and Morin, P.: The Reference Elevation Model of Antarctica - Mosaics, Version 2, Harvard Dataverse [data set], <https://doi.org/10.7910/DVN/EBW8UC>, 2022.
- Huang, Z., Wang, S., Alley, R. B., and Parizek, B. R.: A robust multitask deep learning algorithm for Antarctic ice shelf fracture detection from multisource satellite imagery, *Remote Sensing of Environment*, 330, 114964, <https://doi.org/10.1016/j.rse.2025.114964>, 2025.



- Huang, Z., Wang, S., Alley, R., Li, A., and Parizek, B.: A Novel Deep Learning-Based Approach for Rift and Iceberg
715 Recognition From ICESat-2 Data, *IEEE Transactions on Geoscience and Remote Sensing*, 62, 4300917,
<https://doi.org/10.1109/tgrs.2024.3382573>, 2024.
- Hulbe, C., LeDoux, C., and Cruikshank, K.: Propagation of long fractures in the Ronne Ice Shelf, Antarctica, investigated
using a numerical model of fracture propagation, *Journal of Glaciology*, 56, 459–472,
<https://doi.org/10.3189/002214310792447743>, 2010.
- 720 Izeboud, M. and Lhermitte, S.: Damage detection on Antarctic ice shelves using the normalised radon transform, *Remote
Sensing of Environment*, 284, 113359, <https://doi.org/10.1016/j.rse.2022.113359>, 2023.
- Izeboud, M., Wouters, B., de Roda Husman, S., and Lhermitte, S.: Damage development on Antarctic ice shelves sensitive
to climate warming, *Nature Climate Change*, 15, 1333–1339, <https://doi.org/10.1038/s41558-025-02453-4>, 2025.
- Jin, J., Payne, A., and Bull, C.: Current reversal leads to regime change in the Amery Ice Shelf cavity in the 21st century,
725 *Cryosphere*, 19, 1873–1896, <https://doi.org/10.5194/tc-19-1873-2025>, 2025.
- Joughin, I., Shapero, D., Smith, B., Dutrieux, P., and Barham, M.: Ice-shelf retreat drives recent Pine Island Glacier speedup,
Science Advances, 7, eabg3080, <https://doi.org/10.1126/sciadv.abg3080>, 2021.
- King, E. C., De Rydt, J., and Gudmundsson, G. H.: The internal structure of the Brunt Ice Shelf from ice-penetrating radar
analysis and implications for ice shelf fracture, *Cryosphere*, 12, 3361–3372, <https://doi.org/10.5194/tc-12-3361-2018>, 2018.
- 730 Lai, C., Kingslake, J., Wearing, M., Chen, P., Gentine, P., Li, H., Spergel, J., and van Wessem, J.: Vulnerability of
Antarctica's ice shelves to meltwater-driven fracture, *Nature*, 584, 574–578, <https://doi.org/10.1038/s41586-020-2627-8>,
2020.
- Lhermitte, S., Sun, S., Shuman, C., Wouters, B., Pattyn, F., Wuite, J., Berthier, E., and Nagler, T.: Damage accelerates ice
shelf instability and mass loss in Amundsen Sea Embayment, *Proceedings of the National Academy of Sciences of the
735 United States of America*, 117, 24735–24741, <https://doi.org/10.1073/pnas.1912890117>, 2020.
- Li, G., Guo, J., Pei, L., Zhang, S., Tang, X., and Yao, J.: Extraction and Analysis of the Three-Dimensional Features of
Crevasses in the Amery Ice Shelf Based on ICESat-2 ATL06 Data, *IEEE Journal of Selected Topics in Applied Earth
Observations and Remote Sensing*, 14, 5796–5806, <https://doi.org/10.1109/jstars.2021.3085302>, 2021.
- Li, Q., Wang, Z., An, J., and Zhang, B.: Three-Dimensional Characterization of Pan-Antarctic Ice Shelf Fracture: An
740 Integrated Deep Learning and Hydrological Analysis Framework, *IEEE Geoscience and Remote Sensing Letters*, 22, 1–5,
<https://doi.org/10.1109/lgrs.2025.3595934>, 2025a.
- Li, Q., Wang, Z., An, J., Liu, M., Jiang, P., and Shi, Z.: Assessment of Larsen C Ice Shelf stability: insights from surface and
basal fracture, *International Journal of Digital Earth*, 18, 2475165, <https://doi.org/10.1080/17538947.2025.2475165>, 2025b.
- Li, Q., An, J., Xing, Z., Wang, Z., Jiang, P., Yan, B., Wu, Y., and Zhang, B.: Three-dimensional dynamic monitoring of
745 crevasses based on deep learning and surface elevation reconstruction methods, *International Journal of Applied Earth
Observation and Geoinformation*, 132, 104017, <https://doi.org/10.1016/j.jag.2024.104017>, 2024a.



- Li, T., Heidler, K., Mou, L., Ignéczi, A., Zhu, X., and Bamber, J.: A high-resolution calving front data product for marine-terminating glaciers in Svalbard, *Earth System Science Data*, 16, 919–939, <https://doi.org/10.5194/essd-16-919-2024>, 2024b.
- Lilien, D., Joughin, I., Smith, B., and Shean, D.: Changes in flow of Crosson and Dotson ice shelves, West Antarctica, in response to elevated melt, *Cryosphere*, 12, 1415–1431, <https://doi.org/10.5194/tc-12-1415-2018>, 2018.
- 750 Lv, D., Cheng, Y., Xiao, H., and Hai, G.: A Framework for Fracture Extraction Under Glaciological Property-Based Constraints: Scientific Application on the Filchner-Ronne Ice Shelf of Antarctica, *Earth and Space Science*, 9, e2022EA002293, <https://doi.org/10.1029/2022ea002293>, 2022.
- Marsh, O., Arthern, R., and De Rydt, J.: Ocean tides trigger ice shelf rift growth and calving, *Nature Communications*, 16, 6697, <https://doi.org/10.1038/s41467-025-61796-w>, 2025.
- 755 Miles, B., Li, T., and Bingham, R.: Totten Ice Shelf history over the past century interpreted from satellite imagery, *Cryosphere*, 19, 4027–4043, <https://doi.org/10.5194/tc-19-4027-2025>, 2025.
- Miles, B. W. J. and Bingham, R. G.: Progressive unanchoring of Antarctic ice shelves since 1973, *Nature*, 626, 785–791, <https://doi.org/10.1038/s41586-024-07049-0>, 2024.
- 760 Morris, A., Lipovsky, B., Walker, C., and Marsh, O.: Ice shelf calving due to shear stresses: observing the response of Brunt Ice Shelf and Halloween Crack to iceberg calving using ICESat-2 laser altimetry, satellite imagery, and ice flow models, *Cryosphere*, 19, 4303–4325, <https://doi.org/10.5194/tc-19-4303-2025>, 2025.
- Mouginot, J., Scheuchl, B., and Rignot, E.: MEaSURES Antarctic Boundaries for IPY 2007–2009 from Satellite Radar, Version 2, NASA National Snow and Ice Data Center Distributed Active Archive Center [data set], <https://doi.org/10.5067/AXE4121732AD>, 2017.
- 765 Ochwat, N., Scambos, T., Banwell, A., Anderson, R., MacLennan, M., Picard, G., Shates, J., Marinsek, S., Margonari, L., Truffer, M., and Pettit, E.: Triggers of the 2022 Larsen B multi-year landfast sea ice breakout and initial glacier response, *Cryosphere*, 18, 1709–1731, <https://doi.org/10.5194/tc-18-1709-2024>, 2024.
- Otosaka, I., Shepherd, A., Ivins, E., Schlegel, N., Amory, C., van den Broeke, M., Horwath, M., Joughin, I., King, M., Krinner, G., Nowicki, S., Payne, A., Rignot, E., Scambos, T., Simon, K., Smith, B., Sorensen, L., Velicogna, I., Whitehouse, P., Geruo, A., Agosta, C., Ahlstrom, A., Blazquez, A., Colgan, W., Engdahl, M., Fettweis, X., Forsberg, R., Gallée, H., Gardner, A., Gilbert, L., Gourmelen, N., Groh, A., Gunter, B., Harig, C., Helm, V., Khan, S., Kittel, C., Konrad, H., Langen, P., Lecavalier, B., Liang, C., Loomis, B., McMillan, M., Melini, D., Mernild, S., Mottram, R., Mouginot, J., Nilsson, J., Noël, B., Pattle, M., Peltier, W., Pie, N., Roca, M., Sasgen, I., Save, H., Seo, K., Scheuchl, B., Schrama, E., Schröder, L., 775 Simonsen, S., Slater, T., Spada, G., Sutterley, T., Vishwakarma, B., van Wessem, J., Wiese, D., van der Wal, W., and Wouters, B.: Mass balance of the Greenland and Antarctic ice sheets from 1992 to 2020, *Earth System Science Data*, 15, 1597–1616, <https://doi.org/10.5194/essd-15-1597-2023>, 2023.
- Pang, A., Liang, Q., Li, W., Zheng, L., Li, T., and Cheng, X.: The distribution and evolution of surface fractures on pan-Antarctic ice shelves, *International Journal of Digital Earth*, 16, 3295–3320, <https://doi.org/10.1080/17538947.2023.2246436>, 2023.
- 780



- Pang, A., Liang, Q., Hulbe, C., Yang, T., Zhou, Q., Forbes, M., and Cheng, X.: A Framework for Characterizing 3-D Structures of Crevasses and Rifts Across Antarctic Ice Shelves, *IEEE Transactions on Geoscience and Remote Sensing*, 64, 4300119, <https://doi.org/10.1109/tgrs.2025.3645189>, 2026.
- 785 Qiao, G., Li, Y., Guo, S., and Ye, W.: Evolving Instability of the Scar Inlet Ice Shelf based on Sequential Landsat Images Spanning 2005–2018, *Remote Sensing*, 12, 36, <https://doi.org/10.3390/rs12010036>, 2020.
- Ranganathan, M., Robel, A. A., Huth, A., and Duddu, R.: Glacier damage evolution over ice flow timescales, *Cryosphere*, 19, 1599–1619, <https://doi.org/10.5194/tc-19-1599-2025>, 2025.
- Rignot, E., Mouginot, J., and Scheuchl, B.: MEASUREs InSAR-Based Antarctica Ice Velocity Map, Version 2, NASA National Snow and Ice Data Center Distributed Active Archive Center [data set], <https://doi.org/10.5067/D7GK8F5J8M8R>,
790 2017.
- Spergel, J., Kingslake, J., Creyts, T., van Wessem, M., and Fricker, H.: Surface meltwater drainage and ponding on Amery Ice Shelf, East Antarctica, 1973–2019, *Journal of Glaciology*, 67, 985–998, <https://doi.org/10.1017/jog.2021.46>, 2021.
- Studinger, M.: IceBridge ATM L1B Elevation and Return Strength, Version 2, NASA National Snow and Ice Data Center Distributed Active Archive Center [data set], <https://doi.org/10.5067/19SIM5TXKPGT>, 2013.
- 795 Studinger, M. and Harbeck, J.: IceBridge CAMBOT L1B Geolocated Images, Version 2, NASA National Snow and Ice Data Center Distributed Active Archive Center [data set], <https://doi.org/10.5067/B0HL940D452L>, 2019.
- Surawy-Stepney, T., Hogg, A., Cornford, S., and Davison, B.: Episodic dynamic change linked to damage on the Thwaites Glacier ice tongue, *Nature Geoscience*, 16, 37–43, <https://doi.org/10.1038/s41561-022-01097-9>, 2023a.
- Surawy-Stepney, T., Hogg, A., Cornford, S., and Hogg, D.: Mapping Antarctic crevasses and their evolution with deep
800 learning applied to satellite radar imagery, *Cryosphere*, 17, 4421–4445, <https://doi.org/10.5194/tc-17-4421-2023>, 2023b.
- Surawy-Stepney, T., Hogg, A., Cornford, S., Wallis, B., Davison, B., Selley, H., Slater, R., Lie, E., Jakob, L., Ridout, A., Gourmelen, N., Freer, B., Wilson, S., and Shepherd, A.: The effect of landfast sea ice buttressing on ice dynamic speedup in the Larsen B embayment, Antarctica, *Cryosphere*, 18, 977–993, <https://doi.org/10.5194/tc-18-977-2024>, 2024.
- Tang, L., Bamber, J., Li, T., and Qiao, G.: Surface Damage Dataset for Antarctic Ice Shelves 1999–2024, Zenodo [data set],
805 <https://doi.org/10.5281/zenodo.20425951>, 2026a.
- Tang, L., Bamber, J. L., Qiao, G., and Kong, Y.: A Non-Reference Diffusion-Based Restoration Framework for Landsat 7 ETM+ SLC-off Imagery in Antarctica, *arXiv [preprint]*, arXiv:2605.21371, <https://doi.org/10.48550/arXiv.2605.21371>, 2026b.
- Walker, C., Becker, M., and Fricker, H.: A High Resolution, Three-Dimensional View of the D-28 Calving Event From
810 Amery Ice Shelf With ICESat-2 and Satellite Imagery, *Geophysical Research Letters*, 48, e2020GL091200, <https://doi.org/10.1029/2020gl091200>, 2021.
- Wang, S., Alexander, P., Wu, Q., Tedesco, M., and Shu, S.: Characterization of ice shelf fracture features using ICESat-2-A case study over the Amery Ice Shelf, *Remote Sensing of Environment*, 255, 112266, <https://doi.org/10.1016/j.rse.2020.112266>, 2021.



- 815 Wang, S., Alexander, P., Alley, R., Huang, Z., Parizek, B., Willet, A., and Anandkrishnan, S.: Recent Variability in Fracture Characteristics and Ice Flow of Thwaites Ice Shelf, West Antarctica, *Journal of Geophysical Research: Earth Surface*, 130, e2024JF008118, <https://doi.org/10.1029/2024jf008118>, 2025.
- Wang, Z. and Bovik, A.: A universal image quality index, *IEEE Signal Processing Letters*, 9, 81–84, <https://doi.org/10.1109/97.995823>, 2002.
- 820 Wang, Z., Bovik, A., Sheikh, H., and Simoncelli, E.: Image quality assessment: From error visibility to structural similarity, *IEEE Transactions on Image Processing*, 13, 600–612, <https://doi.org/10.1109/tip.2003.819861>, 2004.
- Xie, E., Wang, W., Yu, Z., Anandkumar, A., Alvarez, J. M., and Luo, P.: SegFormer: Simple and Efficient Design for Semantic Segmentation with Transformers, *Advances in Neural Information Processing Systems*, 34, 12077–12090, 2021.
- Xu, B., Liang, Q., Chang, B., Li, Y., Li, T., Zheng, L., Zhang, W., and Cheng, X.: Extracting Antarctic ice shelf fracture depths using the linear cloth simulation filtering algorithm, *International Journal of Applied Earth Observation and Geoinformation*, 149, 105255, <https://doi.org/10.1016/j.jag.2026.105255>, 2026.
- 825 Zhang, R., Isola, P., Efros, A., Shechtman, E., and Wang, O.: The Unreasonable Effectiveness of Deep Features as a Perceptual Metric, 31st IEEE/CVF Conference on Computer Vision and Pattern Recognition (CVPR), 586–595, <https://doi.org/10.1109/cvpr.2018.00068>, 2018.
- 830 Zhao, J., Liang, S., Li, X., Duan, Y., and Liang, L.: Detection of Surface Crevasses over Antarctic Ice Shelves Using SAR Imagery and Deep Learning Method, *Remote Sensing*, 14, 487, <https://doi.org/10.3390/rs14030487>, 2022.
- Zheng, K., Li, Q., Wang, Z., An, J., Huang, F., Liu, M., and Bao, S.: CREVNet: A Transformer and CNN-Based Network for Accurate Segmentation of Ice Shelf Crevasses, *IEEE Geoscience and Remote Sensing Letters*, 21, 1–5, <https://doi.org/10.1109/lgrs.2024.3407860>, 2024.
- 835 Zhu, Q., Guo, H., Zhang, L., Liang, D., Wu, Z., Liu, Y., and Lv, Z.: GLA-STDeepLab: SAR Enhancing Glacier and Ice Shelf Front Detection Using Swin-TransDeepLab With Global-Local Attention, *IEEE Transactions on Geoscience and Remote Sensing*, 61, 5218113, <https://doi.org/10.1109/tgrs.2023.3324404>, 2023.